Università degli Studi di Pavia


Ph. D. Thesis

# Aspects of Electron Dynamics in Low Dimensional Systems Based on Metal Surfaces and Semiconductor Heterojunctions

*Francesco Banfi*

Università degli Studi di Pavia


Ph. D. Thesis

# Aspects of Electron Dynamics in Low Dimensional Systems Based on Metal Surfaces and Semiconductor Heterojunctions

*Francesco Banfi*

Pavia, 2003

Supervisor

*Prof. Giorgio Guizzetti*

Promotor

*Prof. Fulvio Parmigiani*

*to my dad*

# Contents

# Chapter 1

# Introduction

## 1.1 Overview

The interest in interface and surface physics has grown at a tremendous pace in the last decades, thanks to the availability of novel material processing and growth techniques and the emergence of new spectroscopic methods. The interest is both scientific and technological in nature.

Femtosecond lasers allow to create a transient two-dimensional electron gas (2DEG) at a metal-vacuum interface known as image potential state (IPS) and, together with multi-photon and angle-resolved photoemission spectroscopy (ARPES), to exploit the dynamics of electrons in this states and their interaction with bulk electrons, hence giving new insight in low dimensional and many body physics. Pump and probe techniques permit to follow, in a time-resolved fashion, the electron dynamic of the system to the point where quantum mechanical electron coherency can be exploited. Intriguing phenomena such as above threshold photoionization (ATP) and hot electron population dynamic in metals are related fields that benefit from the above mentioned techniques. Binding energy and life-time investigation of IPS have also proved to be of paramount importance for the study of physisorption and surface photochemistry.

Semiconductor heterojunctions constitute the traditional test bench to explore low dimensional physics. Molecular beam epitaxy (MBE), together with the introduction of modulation-doping, opened the path to the realization of high-mobility 2DEGs. Macroscopic manifestations of quantum-mechanical effects, such as conductance quantization and Quantum Hall (QH) effects just to mention a few, rely on high-mobility 2DEGs. The next step resides in the birth of high-resolution electron-beam lithography (EBL). Patterning of semiconductor-based 2DEGs via EBL is, nowadays, the most versatile technique to achieve lower dimensionality in the form of quantum wires (QW) and quantum dots (QD) of virtually any desired shape. Nanoelectronic devices, based on electron wave function coherency, are the natural outcome of such achievements.

Under an applicative point of view the record and importance of the physics of heterojunctions (both surfaces and interfaces) is unmatched. All microelectronic and solid-state optoelectronic devices rely on semiconductor-semiconductor or metal-semiconductor interfaces. Some of them exploit the advantages of reduced dimensionality. Heterostructure Field Effect Transistor, Modulation Doping Field Effect Transistor, Quantum Well Lasers and, recently, Quantum Cascade Lasers, are just some examples. In this frame, issues concerning surface states are of the utmost importance. Coupling of bulk electrons to surface states and surface recombination can drastically affect transport properties. Surface recombination is a serious concern in that electrons trapped at active surface sites do not contribute to transport. This is true in particular for photovoltaics and devices based on shallow 2DEGs. Furthermore surface reconstruction, endurance and material deposition, clue elements in the electronic industry, belong to the field of studies of surface science.

## 1.2 Purpose and outline of this work

The results presented in this thesis can be ascribed to the context briefly outlined in the overview. The work consists of two main parts, the common features being the 2DEG nature of the systems under investigation and several experimental techniques such as vacuum technology and material processing. The first part deals with electron dynamics in surface-based 2DEGs, addressed as IPS, studied via two-photon photoemission spectroscopy (2PPE) and, as a side product of mastering the experimental technique, ATP in

solids. The second part, more technical in nature, concerns the design and development of new quantum interference devices (QUID). Design and characterization of the heterostructures are presented, together with devices construction schemes and carachterization. In one case preliminary measurement are also reported, indicating the work has been moving on the correct track. A theoretical proposal for a three-dimensional QUID, based on the achieved experience, is also shown and numerically investigated.

# Chapter 2

# Background

## 2.1 Two-photon photoemission spectroscopy of image states

### 2.1.1 *Two-dimensional electron gas at a metal-vacuum interface: image states*

Image potential states (IPS) are an interesting class of surface states, originated by electrons trapped in front of a metal surface when a gap of the projected bulk states occurs at energies below the vacuum level. In this case a high electron reflectivity prevents electrons from decaying into the bulk and a long range binding potential is formed by the Coulomb attraction between electrons in the vacuum and their image charge (see Fig. 2.1) in the solid

$$V(z) = E_{vac} - \frac{e^2}{4\pi\epsilon_0}\frac{1}{(4z)} \tag{2.1}$$

whereas the electron is unbound in the x-y plane parallel to the surface. The eigenvalue problem factorizes in a 2-dimensional free-electron like wavefunction parallel to the surface plane and a bound hydrogen-like wavefunction along the $z$ direction perpendicular to the surface. The wave functions for the perpendicular direction are obtained from the radial part of the wave function for the hydrogen atom multiplied by $z$ (due to the reduced dimensionality) and expanded by a factor

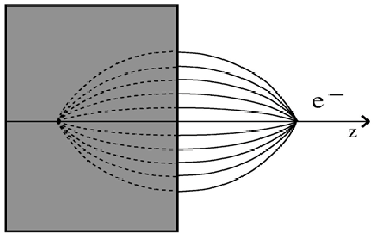


FIGURE 2.1: The figure depicts an electron positioned in front of a metal surface. The metal is represented by the gray slab. Electric field distribution due to an electron in vacuum and its image charge is also reported. The field on the vacuum side of the metal surface (solid lines are field lines in vacuum), due to the presence of the electron, is the same as the field that would be produced by the system comprising an electron and its image charge if the metal was removed.

of 4 (due to the weaker potential) [1, 2], see Fig. 2.2. A universal Rydberg-like binding energy $E(n)$=-Ry/$16n^2$= -0.85 (eV)$n^{-2}$ and a lifetime $\tau_n$ that scales as $\tau_n \propto n^3$, where $n$=0,1,2.. are expected [3]. The Rydberg-like states are called image potential states and, for a fixed value $n$, they constitute a 2DEG.

### 2.1.2 *Two-photon photoemission spectroscopy*

Electronic states in solids and at solids surfaces have been studied extensively by photoemission measurements. If the photon energy $h\nu$ is known and the kinetic energy $E$ of the photoelectron is measured, the energy of the initial state $E_i$ with respect to the vacuum energy $E_{vac}$ is determined. If the work function $\Phi$ is known, information on the energy position of $E_i$ with respect to the Fermi level $E_F$ can be obtained. The emission spectrum is a picture of the density of the initial states, provided the final states form a smooth continuum and the transition probability is homogeneous. The energy range accessible to traditional one-photon photoelectron spectroscopy is limited to initial states below $E_F$ and to final states above $E_{vac}$.

In order to investigate the unoccupied states, in particular those lying in the range comprised among $E_F$ and $E_{vac}$, either inverse photoemission or two-photon photoemission spectroscopy is used. Inverse photoemission is the time-reversal of standard photoemission: impinging electrons are used and the emitted photons are recorded (see left scheme in Fig. 2.3). This technique suffers of low resolution, the energy spread of the electron beam being $\sim$ 100 meV. Two-photon

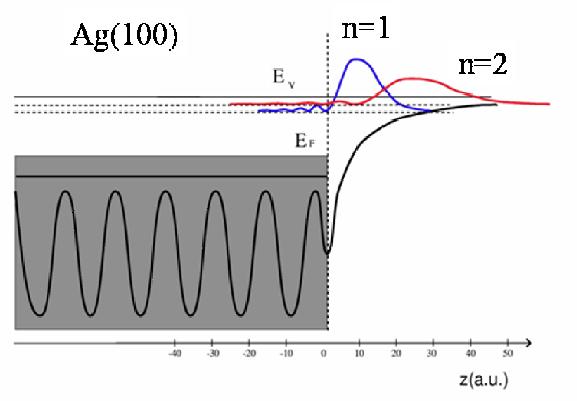


FIGURE 2.2: Wave function component along the z direction. Two eigenfunctions are shown relative to the $n$=1 and $n$=2 IPS. Both eigenvalues fall in the energy gap. The $n$=1 and $n$=2 eigenvalues are represented by the dotted line. The black line, oscillating in the bulk and hydrogen-like in vacuum, is a model potential energy. The figure has been taken from [4].

photoemission overcomes this problem. In 2PPE the first photon excites an electron from the initial state $E_i$ to an intermediate state $E_m$, from where a second photon brings the electron to the final state above $E_{vac}$. This is represented in the middle scheme of Fig. 2.3, where $E_m$ coincides with the $n$=1 IPS.

The width of a peak in 2PPE can be related to the lifetime of the corresponding state. In case the width of the analyzer function is comparable to the intrinsic line width, the lifetime can be accessed by line-profile analysis. Another experimental technique allowing to measure intermediate states lifetimes is time-resolved photoemission spectroscopy. A pump pulse populates the intermediate state, whereas the probe pulse ionizes it. Delaying the probe pulse with respect to the pump pulse reduces the measured photoemitted electrons count rate and provides a direct measurement of the life time. The concepts here reported have been taken from a very good review. I suggest it for a through and extensive treatment of the subject [5].

Multi-photon photoemission spectroscopy comprises also the non-resonant coherent photoemission case. In this case an electron absorbs $n$ photons (two photons in the case of 2PPE) of energy $h\nu \leq \Phi$ and, provided $nh\nu \geq \Phi$, where $\Phi$ is the work function, is emitted in vacuum. Refer to right scheme in Fig. 2.3.

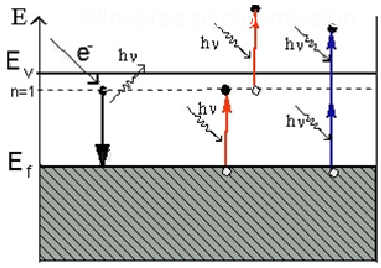


FIGURE 2.3: Inverse photoemission and 2PPE processes. The left scheme illustrates the basic concepts involved in inverse Photoemission. The central scheme illustrates a 2PPE resonant process. The right scheme illustrates non-resonant coherent 2PPE.

### 2.1.3 *Angle-resolved photoemission spectroscopy and its application to the study of image potential states*

In order to investigate the dispersion of the IPS electronic bands $E_n(\mathbf{k}_\parallel)$, it is necessary to determine the electron wave vector component $k_\parallel$. This requires the experimental determination of the electron kinetic energy together with the electron emission direction by means of an electron energy analyzer with small angular aperture. The kinetic energy of the photoemitted electron $E_{kin}$ and the angle $\theta$, $\theta$ is the angle between the emission direction and the surface normal, are measured. The wave-vector component of the photoemitted electron parallel to the crystal surface is $k_\parallel^{ex}$. Because of two-dimensional (2D) translational symmetry, the wave-vector component parallel to the surface is conserved in the transition from the image-state to the vacuum, that is $\mathbf{k}_\parallel = \mathbf{k}_\parallel^{ex}$. Hence, one accesses $E_{\mathbf{k}\parallel}$. This technique is known as angle-resolved photoemission spectroscopy (ARPES).

### 2.1.4 *General experimental considerations*

A schematic description of the apparatus for 2PPE and nPPE is here reported. Further details on the actual experimental set-up will be pointed out case-by-case when discussing the experiments. The experimental arrangement consists of three stages, namely, laser source and optics, ultra-high vacuum chamber, together with equipment for surface preparation and analysis, and, finally, an electron energy analyzer. Multi-photon photoemission is a non-linear process, hence high laser intensities are needed. This requires a pulsed laser source. In order to access the required photon energies, non-linear optical techniques are used such as higher harmonic generations and

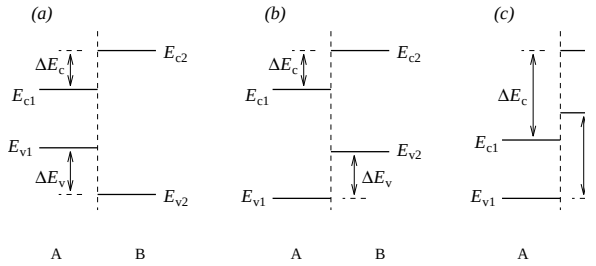


FIGURE 2.4: Heterojunctions of type (a)I, (b)III and (c)II are reported. A and B label the two different materials constituting the heterojunction. Valence band offset $\Delta E_v$ and conduction band offset $\Delta E_c$ are also shown.

optical parametric down-conversion. The vacuum chamber has three working stages. At the sample preparation stage (higher stage), sputtering, by means of an ion gun, and annealing of the sample are performed. At the sample analysis stage (middle stage), low-energy electron-diffraction (LEED) pattern are performed in order to check for proper surface reconstruction and orientation. The experimental stage comprises an entrance window for the laser beam and a collection path for the photoemitted electrons. The sample holder is mounted on a manipulator with 5 degrees of freedom. The energy analyzer used in this thesis work is a time-of-flight (TOF) spectrometer.

## 2.2 Quantum interference devices

### 2.2.1 *Two-dimensional electron gas at a semiconductor-semiconductor heterojunction*

The advent of MBE opened the path to band-edge engineering. Consider two semiconductor materials with similar lattice parameters, such as $GaAs$ and $AlGaAs$. Joining the two semiconductors, band alignment occurs so as to guarantee a constant chemical potential throughout the entire structure. Three types of heterojunctions are reported in Fig. 2.4. Let's consider the case of a $GaAs$-/$Al_xGA_{1-x}As$ heterojunction (case (a) in Fig. 2.4), $x$ being the $Al$ mole fraction. Changing the $Al$ mole fraction $x$, changes the relative energy height among the $Al$ and $Al_xGa_{1-x}As$ bands,thus allowing to tailor the desired band profile.

A major advance came with the introduction of *n-type* modulation-doped samples [6]. In this

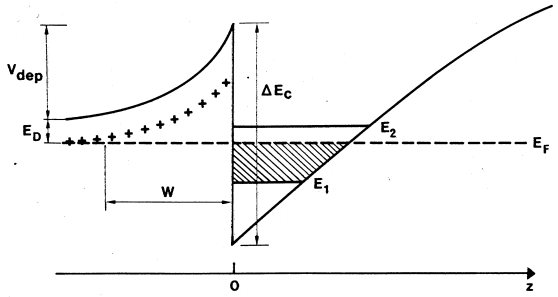


FIGURE 2.5: Band diagram at a *GaAs-AlGaAs* heterojunction. $E_1$ and $E_2$ are the eigenvalues constituting the $n$=1 and $n$=2 2DEGs. $E_F$ is the Fermi level or, more correctly, the chemical potential. Note that, in the present case, only the 2DEG $n$=1 is occupied, in fact $E_1$ is energetically smaller than $E_F$. $\Delta E_c$ is the conduction band offset, $W$ is the depletion layer and $V_{dep}$ the depletion potential. Figure taken from Ref. [7].

technique the *AlGaAs* part of the heterojunction is *n-doped* and the doped layer is separated by an undoped slice of *AlGaAs* from the heterojunction. In so doing electrons transfer to the *GaAs* layer until an equilibrium is reached. Solution of the self-consistent Poisson-Schrödinger problem yields to the band-diagram reported in Fig. 2.5. In this way a potential barrier is formed on the *GaAs* side of the interface tightly confining the electrons. The electronic eigenvalue problem has quantized energy solutions very similar to the one typical of a triangular-well. Each quantized level is referred as a subband or 2DEG. The electrons are confined in a direction perpendicular to the heterojunction and are free to move in a plane parallel to the heterojunction plane, in a way very similar to the IPS case. Note that the electrons are physically separated by the ionized donors, hence carrier scattering probability s greatly reduced as compared to the situation where the bulk semiconductor is normally doped. This fact enhances electron mobility by order of magnitudes.

### 2.2.2 *Shubnikov-de Haas and Hall effects*

Consider a 2DEG in a perpendicular magnetic field **B**. With reference to an Hall bar geometry, were a constant current $I$ is flowing along the longitudinal direction, the following definitions apply: $V_{xx}$ and $V_{xy}$ are the longitudinal and the transverse voltages respectively; the longitudinal resistance is defined as $R_{xx} \equiv \mathrm{V}_{xx}/I$, whereas the transverse resistance is defined as $R_{xy} \equiv \mathrm{V}_{xy}/I$. The Hall coefficient $R_H$ is defined as $R_H \equiv \mathrm{R}_{xy}/B = 1/en_e$ and has dimensions $\Omega$/Tesla. The

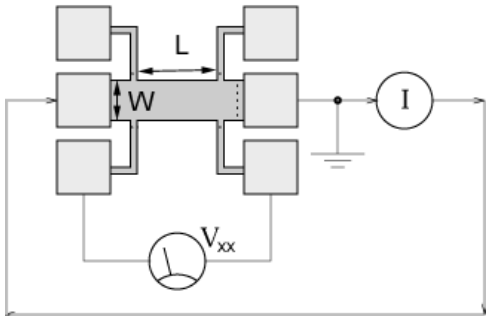


FIGURE 2.6: Set up for SdH measurement. A DC current $I$ is forced through the sample and the voltage $V_{xx}$ is measured. In actual measurements the current $I$ is supplied at a frequency of 17.3 Hz and $V_{xx}$ is detected with a lock-in technique.

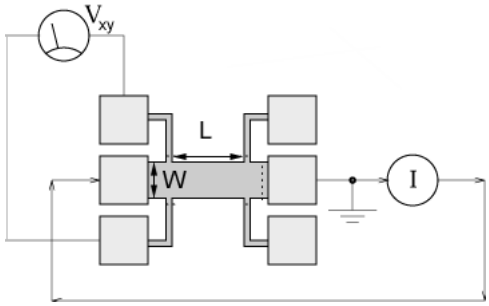


FIGURE 2.7: Set up for Hall measurement. A DC current $I$ is forced through the sample and the voltage $V_{xy}$ is measured. In actual measurements the current $I$ is supplied at a frequency of 17.3 Hz and $V_{xy}$ is detected with a lock-in technique.

voltage probes are separated by $L$, whereas the Hall bar width is $W$. Refer to Figures 2.6, 2.7.

Sweeping the magnetic field $\mathbf{B}$, oscillations in $R_{xx}$, with a period of $1/B$, arise. This evidence is known as Shubnikov-de Haas (SdH) effect. The electron sheet density of the 2DEG is defined as $n_e$ ($m^{-2}$). In the above mentioned situation the energy spectra of the 2DEG results in Landau levels:

$$E_n = \hbar\omega_c(n + 1/2) \tag{2.2}$$

$\omega_c$ being the cyclotron frequency $eB/m^*$, with $m^*$ the electron effective mass. Each Landau level has a degeneracy per unit $N(B)$=$2eB/h$ (spin degrees of freedom are degenerate in this formula). In magneto-transport all measurement are performed at cryogenic temperatures and applying very small excitation voltages (quasi-equilibrium), so that all the electrons involved in the transport process are at the Fermi energy. In this situation the Landau levels are filled in increasing order and the integer part of $n_e/N(B)$ represents the index of the uppermost fully occupied Landau level. Two situations are possible: (a) the next (energy-wise) Landau level is partially occupied, (b) the next Landau level is empty . In case (a) scattering events are very likely to occur because many empty states are accessible and very close in energy to the occupied ones. In case (b), that is when the equation $n_e$=$iN(B)$ is fulfilled for an integer value of $i$, a minimum in resistance occurs. The condition for this occurrence can be casted in the form:

$$B = n_e h/2ei. \tag{2.3}$$

The resistance $R_{xx}$ then oscillates versus $1/B$, and, indicating $\Delta(1/B)$ the oscillation period, one recovers the 2DEG sheet electron charge density $n_e$ from

$$n_e = \frac{2e}{h\Delta(1/B)}. \tag{2.4}$$

When more than one subband is populated, several oscillation frequencies are obtained performing the Fourier transform of the ($R_{xx}$(B), B) data set. The density of each subband can then be determined from equation 2.4.

Another effect that arises when a 2DEG is positioned in a perpendicular magnetic field **B** is the Hall effect. The range of field intensities $B$ for the Hall effect to be observable is lower than the range of field intensities required for the observation of SdH oscillations. The SdH effect requires the appearance of Landau levels, where is the classical Hall effect occurs when the density-of-states (DOS) is still of the pure 2DEG kind (magnetic field not appreciably affecting the DOS). The Hall effect is rather well known so I will only report the two relations allowing to access the average electron charge and the electron mobility of a 2DEG:

$$n_e = \frac{BI}{eV_{xy}} \tag{2.5}$$

Measurement of the electron conductivity $\sigma$ allows to access the electron mobility $\mu$=$\sigma/ne$. In terms of the Hall bar geometric parameters:

$$\mu = \frac{L}{W}\frac{I}{V_{xx}}\frac{1}{en_e} = \frac{L}{W}\frac{V_{xy}}{V_{xx}}\frac{1}{B} \tag{2.6}$$

### 2.2.3 *Nanopatterning, lateral confinement and the quantum wire*

Further reduction in dimensionality can be achieved by patterning on a nanometric scale the 2DEG. This can be achieved by several methods [8]. In this thesis work, nanopatterning has been performed using lithographic techniques and gating methods. Further details can be found in Appendix A.

The reduction in dimensionality, in the present work, is from two to one dimension. An electron in a quantum wire is bound by a potential well in two dimensions and is free to propagate in the third one. A great number of effects arise because of this reduction in dimensionality [7]. In the frame of coherent transport properties, tailoring the lateral confinement and/or the electron density in the QW allows to tune the number of propagating modes [9], [10]. The situation is very much like at what occurs in optical wave guides.

### 2.2.4 *Transport in mesoscopic systems*

Semiconductor devices presented here are based on high mobility 2DEG. At cryogenic temperature and with a small enough applied bias $V$ ($eV \ll \mathrm{k}_B T$) electron transport is ballistic on the length-scale of the order of one micron. In this regime Landauer formalism applies [9], [10], [11]. Conductance $G$ is given by $G{=}2e^2T/h$, $T$ being the electron wave function transmission for the device portion under investigation calculated at the Fermi Level. As already mentioned, the situation is analogous to what is usually encountered in electro-magnetic waves propagation in wave-guiding media [12]. The above-mentioned formula for conductance applies in a two-probe measurement. In a four-probe measurement it has to be corrected to keep into account the voltage drop that occurs at the emitter/lead and collector/lead junctions, thus giving a measured $G{=}2e^2T/hR$, $R$ being the reflection coefficient calculated at the Fermi energy. Note that when $T$ is very small the two-probe and four-probe formulas coincide. The value $2e^2/h$ is of fundamental importance and is called the conductance quantum[1]. The conductance in a quantum point contact (QPC) is quantized in step of height $2e^2/h$; an example of such conductance quantization is shown in a measurement reported in chapter 7.

[1] $h/2e^2 = 12.8\ \mathrm{k}\Omega$

# Chapter 3

# Measurements of intrinsic linewidth versus parallel momentum of IPS on Ag(100)

Intrinsic linewidths of electronic image-potential states versus the momentum parallel to the surface on Ag(100) have been measured with angle resolved two-photon photoemission using the time of flight technique. The influence of the time of flight spectrometer angular acceptance on intrinsic linewidth measurements is taken into account and a proper data analysis is proposed. The inverse linewidth as a function of parallel momentum is compared with time-resolved measurements of image-state lifetimes on Cu(100) reported in the literature. The data analysis shows that decay dynamics of image potential states in Ag and Cu may be determined by different physical mechanisms.

## 3.1 Motivation

IPS have been investigated using a variety of experimental techniques, such as low-energy-electron diffraction [13], inverse photoemission [14], and scanning tunneling microscopy [15]. Recently, two-photon photoemission (2PPE) spectroscopy [16, 17] has been combined with high resolution electron spectrometers to significantly improve energy and momentum resolution in the investigation of IPS. Moreover, the possibility of probing the IPS population directly in the time domain with pump and probe techniques has greatly enhanced the accuracy of lifetime measurements of long lived IPS states [18, 19].

Relaxation processes of IPS are very important for the study of surface phenomena, such as electronically induced adsorbate reactions or electron transfer across interfaces [20, 21]. Electrons excited in IPS states are subject to decay due to scattering with electrons in the underlying bulk states. These scattering processes, due to the overlapping between the image state wave function and bulk states [3], can be classified in *interband* and *intraband* processes. The final state of the *intraband* process is an IPS state whereas the final state of the *interband* decay channel is a bulk state [22]. As a general rule, a broadening of the intrinsic linewidth with respect to normal emission ($k_{\|}$=0) is observed when a IPS is measured at a parallel momentum different from zero. The $k_{\|}$-dependence of the broadening is different for *interband* and *intraband* processes. In this frame knowledge of the intrinsic linewidth as a function of parallel momentum helps discriminating which mechanism contribute to the IPS decay. Since IPS are a promising model system for a detailed understanding of fundamental mechanism of electron dynamics at surfaces, such measurements may contribute to the development of refined theoretical models.

In this work the intrinsic linewidths ($\gamma$) of IPS on Ag(100) at different $k_{\|}$ values are measured by angle-resolved 2PPE. The inverse linewidth is defined through the relation $\tau=\hbar/\gamma$ ($\hbar$=658meV fs). To achieve a better estimate of the intrinsic linewidth a new fitting procedure, that accounts for the influence of the angular acceptance of the detector, is proposed. The prediction of this improved fitting procedure are tested comparing measurements taken with two Tof that have different angular resolution. The estimated inverse linewidth depends on inelastic scattering processes, that cause the decay of the IPS population, and on quasielastic scattering processes, that destroy the phase relations between

the involved states but do not change the population of the IPS [3, 23]. Comparing the measured inverse linewidth at $k_{\parallel}$=0 with the population lifetime measured directly with time resolved pump and probe experiments on Ag(100) [19], we find the same numerical value. Therefore, in the present work, the quasielastic scattering at $k_{\parallel}$=0 has a negligible contribution.

Recently, the dependence of the lifetime of electrons in the n=1 IPS of Cu(100) on the momentum parallel to the surface has been studied in the time domain, by means of pump and probe 2PPE [22]. These results, together with a theoretical analysis of the problem, indicate that intraband scattering processes mainly contribute to the lifetimes of these states. A critical comparison with the inverse linewidth data on Ag(100) obtained in this work, indicates that different scattering mechanisms may be responsible for population decay in these two metals.

## 3.2 Description of the experimental set-up

The experiments are carried out on an Ag single-crystal, oriented along the (100) surface, kept in a $\mu$ -metal ultra-high vacuum chamber with a base pressure of 2x10$^{-10}$ mbar at room temperature. The sample surface is cleaned by cycles of Ar+ sputtering and subsequent annealing at 400 K. A good LEED pattern is observed after these cycles. Moreover, the quality of the surface is probed by measuring the work function value, which is very sensitive to the cleaning and reconstruction of the surface. It is measured using the fourth harmonic ($h\nu$=6.28eV) of the fundamental wavelength ($h\nu$=1.57 eV) of the Ti:Sapphire system used in these experiments. The low-energy cutoff of the spectra obtained with single photon photoemission are used as a reference for work function measurements. The measured work function is 4.3±0.1 eV. The light source used to excite the IPS is a traveling-wave optical parametric generator (TOPG) pumped by an amplified Ti:Sapphire laser system. The fourth harmonic of the TOPG spans the ultraviolet (UV) photon energy range 3.1-4.4 eV with a pulse time width of 150 fs at 1 kHz repetition rate. The spectra are obtained using an incident p-polarized radiation with photon energy of 4.32 eV at an incident angle of 30°. The kinetic energy of the photoemitted electrons is measured by two time of flight (ToF) spectrometers, characterized by different geometrical acceptance

angle. The low-resolution ToF has an acceptance angle of $\pm 2.6^\circ$, a temporal resolution of 0.5 nsec, and an estimated total energy resolution of 45 meV. The high resolution ToF has an acceptance angle of $\pm 0.83^\circ$, a temporal resolution of 0.25 nsec, and a total energy resolution of 35 meV.

## 3.3 Results and discussion

In Fig. 3.1 the 2PPE spectra at a photon energy of 4.32 eV and at $k_\parallel$=0 with the high resolution ToF (a) and with the low resolution ToF (b), respectively, are shown.

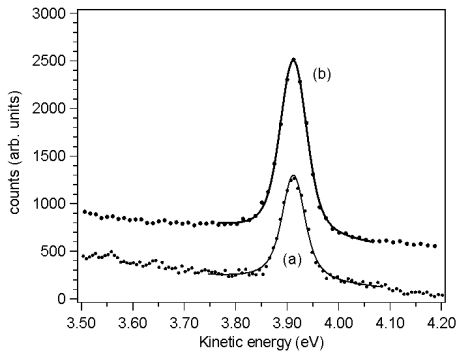


FIGURE 3.1: Two-photon-photoemission spectra at a photon energy of 4.32 eV and at $k_\parallel$=0 collected with the high resolution (a) and the low resolution ToF (b). The feature at about 3.9 eV kinetic energy is ascribed to the n=1 image potential state. The lines represent the fit of the n=1 IPS with a lorentzian convoluted with a gaussian.

The effective mass associated with the n=1 IPS electrons have been measured in a previous work along the direction of the surface Brillouin zone (SBZ), resulting in a value of 0.97±0.02 in free-electron mass units [17]. The binding energy [1] of n=1 IPS feature is 0.4±0.1eV in agreement with the values reported in the literature [3]. The two sets of photoemission measurements are collected by changing the angle between the normal to the sample and the ToF axis, along the $\overline{\Gamma X}$ symmetry direction of the Ag(100) SBZ in

[1] the binding energy is measured with respect to the vacuum level

order to trace the $k_{\|}$-dispersion of the IPS states [17]. In order to estimate the intrinsic linewidth, a study of the lineshape of these states is presented. In particular, the n=1 IPS feature is fitted with a lorentzian convoluted with a gaussian. The linewidth of the lorentzian is considered as a parameter in the fit, whereas the gaussian linewidth ($\sigma$), which accounts for instrumental resolution, has been estimated for both ToF spectrometers and kept fixed. The gaussian linewidth depends on the spectrometer resolution and the laser linewidth. The laser linewidth is the same for the two set of measurements: about 12 meV. The spectrometer resolution depends on the geometrical area of the multichannel plate and on the electronics temporal resolution. The estimated linewidth of the gaussian is about 45meV for the low resolution ToF and 35meV for the high resolution spectrometer. These values are confirmed by fitting the Fermi-edge measured with single photon photoemission at a photon energy of 6.28 eV on Ag(100) cooled at 160K. An isotropic emission of the photoelectrons is considered in the following. Once the gaussian linewidth is fixed, the intrinsic lorentzian linewidth is estimated by the fit.

In Fig. 3.2, the behavior of the intrinsic linewidths against the parallel energy is showed for the two sets of experiments (a,c). The parallel energy is calculated using the following relations:

$$E_{\|} = \frac{\hbar^2 k_{\|}^2}{2m^*} \tag{3.1}$$

$$k_{\|} = \frac{\sqrt{2m^* E_{kin}}}{\hbar} \sin\theta \tag{3.2}$$

where $E_{kin}$ is the photoelectron kinetic energy and $\theta$ is the angle between the perpendicular to the sample and the ToF. The intrinsic linewidth measured at $k_{\|}$=0 with the high resolution ToF (15±2 meV) is in agreement with that obtained with the low resolution ToF (14±2 meV). The inverse linewidth (47±7 fs), is in agrement with time-resolved measurements on Ag(100) previously reported in literature [19]. At $k_{\|}$=0.14 $\mathring{A}^{-1}$, which corresponds to an angle of 8°, the intrinsic linewidth measured with the high resolution ToF is about 20 meV smaller than the value measured with the low resolution ToF. The slope of the best linear fit of $E_{\|}$-dependent intrinsic linewidth obtained with the low resolution ToF is 400±0 meV/eV, whereas the slope with the high resolution ToF is about 150±40 meV/eV (Fig. 3.2). The difference of linewidths of the two measurements (using

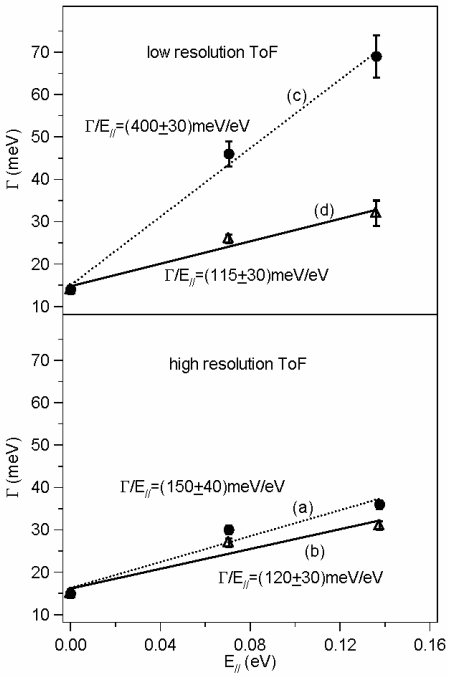


FIGURE 3.2: The behavior of the intrinsic linewidth against the parallel energy is shown for the high and the low resolution ToF by fitting the IPS lineshape with a lorentzian convoluted with a gaussian ((a) and (c)) and with an integral of lorentzians convoluted with a gaussian ((b) and (d)). The lines represent the best linear fit of the experimental data (markers). The slopes are reported in the figure.

high and low resolution ToF) can be ascribed to a spread in $k_{\|}$. The geometrical acceptance angle of the ToF implies that, at a specified angle, the ToF simultaneously collects photoelectrons with different $k_{\|}$-vector, see Fig. 3.3.

In particular, for the low resolution ToF the maximum $\Delta k_{\|}$ spread is about 0.045 $\mathring{A}^{-1}$, whereas for the high resolution ToF $\Delta k_{\|}$ is about 0.015 $\mathring{A}^{-1}$. Therefore, each spectrum is expressed as a sum of lorentzians with different $k_{\|}$. Due to the parabolic $k_{\|}$ dispersion, each of these lorentzian correspond to a different kinetic energy value. To reconcile the

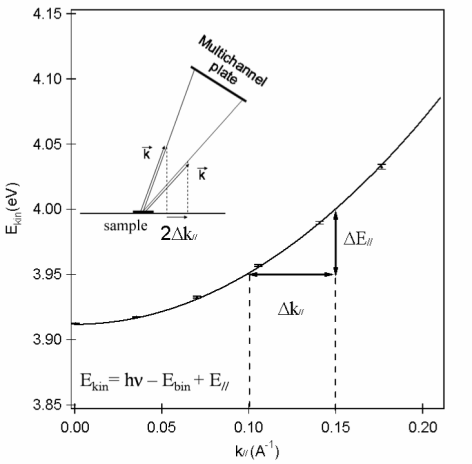


FIGURE 3.3: In this figure the $k_\parallel$-spread related to the geometrical acceptance angle of the low resolution ToF detector is shown. At a specified angle, the detector collects photoelectrons with a different $k_\parallel$, therefore a sum of lorentzians each for a different $k_\parallel$ in the $k_\parallel$ range has to be considered in the fitting procedure. Due to the parabolic behavior of the kinetic energy versus $k_\parallel$, the $E_\parallel$-spread related to the $\Delta k_\parallel$ increases with $k_\parallel$. In the figure the experimental data (markers) are fitted with a parabolic curve (solid line), as discussed in Ref. [17].

intrinsic linewidth values measured with the two spectrometers, the IPS feature has to be fitted with a convolution of a gaussian with a sum of lorentzians. The sum of lorentzians can be expressed as:

$$f(E) = \frac{1}{E_2 - E_1} \int_{E_1}^{E_1} \frac{fwhm}{2} \frac{1}{(E - E_0)^2 + (\frac{fwhm}{2})^2} dE_0 \tag{3.3}$$

that gives

$$f(E) = \frac{1}{\pi(E_2 - E_1)} \left[ -\arctan \frac{E - E_2}{\frac{fwhm}{2}} + \arctan \frac{E - E_1}{\frac{fwhm}{2}} \right] \tag{3.4}$$

where $fwhm$ is the full width at half maximum of the single $k_\parallel$-lorentzian, that is considered constant in the $k_\parallel$ range, $E_0$ is the energy position of the lorentzian, $E_1 = \hbar^2(k_\parallel - \Delta k_\parallel)^2/2m$ and $E_2 = \hbar^2(k_\parallel + \Delta k_\parallel)^2/2m$. Using this fitting procedure the in-

trinsic IPS linewidths at $k_{\parallel}$=0 are in agreement with the previous results, confirming that the $k_{\parallel}$-spread is not relevant at $k_{\parallel}$=0. The intrinsic linewidths at $k_{\parallel} \neq 0$ result the same, within the errors, for both high and low resolution ToF (Fig. 3.2 (b,d)). The slope of the solid lines which represents the best linear fit of the IPS linewidths versus $E_{\parallel}$ is 120 30meV/eV and 115 30meV/eV for high and low resolution ToF, respectively. This slope is comparable with the slope obtained by the high resolution ToF using the single lorentzian fit (150 40meV/eV). Therefore, the contribution of the $k_{\parallel}$-spread in the IPS intrinsic linewidth measurement, can be neglected when the geometrical angular acceptance of the ToF implies a $k_{\parallel}$-spread of about 0.015 $\AA^{-1}$.

The measured slope of the linewidth broadening in Ag(100) as a function of $E_{\parallel}$ ($d\Gamma /dk_{\parallel}$=120 meV/eV) gives an interesting hint when compared to the inverse lifetime ($\gamma$=$\hbar/\tau$ ) broadening measured on Cu(100) using time-resolved 2PPE ($d\Gamma /dk_{\parallel}$=47 meV/eV) [22]. Theoretical calculations for Cu(100) evidence that the contribution of *intraband* scattering must be taken into account to reconcile theory with the measured value of inverse lifetime vs parallel momentum broadening rate. In Ag(100) we find a much more rapid broadening rate, indicating that a different decay dynamics must be considered in evaluating the IPS relaxation in this case. This finding can be related to the presence of a collective excitation (surface plasmons) in Ag(100) that constitutes an important decay channel for IPS. At $k_{\parallel}$=0, the surface plasmon contribution to the decay of Ag(100) IPS is greatly diminished due to a subtle effect originating from the non-local character of the electronic self-energy [24], resulting in a longer lifetime of the IPS than would be expected considering the plasmon decay channel without the non-local correction. The high linewidth broadening rate measured in this work is consistent with a less effective quenching mechanism of the surface plasmon decay channel due to nonlocality at $k_{\parallel}$≠0. Another possible contribution to the different linewidth broadening could be an increase with parallel momentum of quasi-elastic processes. These mechanisms can influence inverse linewidth estimations, while do not contribute to lifetime measured by pump-probe techniques.

## 3.4 Conclusions

The intrinsic linewidths of the electrons in the n=1 IPS on Ag(100) have been measured at different values of the parallel momentum. The spread in $k_{\parallel}$, due to the geometrical acceptance angle of the ToF, have been taken into account. The value of the inverse linewidth of n=1 IPS at $k_{\parallel}$=0 (47±7 fs) is in agreement with the value measured with time-resolved techniques (55±5 fs)[19]. This confirms the validity of our procedures and the fact that, at $k_{\parallel}$=0, the contribution to the linewidth due to quasi-elastic scattering can be neglected. Our experiment evidences a much more rapid intrinsic linewidth broadening versus $E_{\parallel}$ on Ag(100) with respect to Cu(100), indicating that further theoretical investigation is needed to assess the IPS decay mechanism in Ag(100).

# Chapter 4

# Non-resonant multiphoton excitation of IPS and violation of the electric dipole selection rules in Ag(100)

Photoemission from image potential states on Ag(100) is investigated using angle resolved multiphoton photoemission induced by 150 fs laser pulses. For the first time it is shown that image potential states populated by indirect transitions can be observed with light polarized parallel to the plane of incidence and light polarized normal to the plane of incidence. The latter is a process normally forbidden by the dipole transition selection rules. These findings are related to the creation of a hot electron population whose properties

largely remains to be understood.

## 4.1 Motivation

So far the electron dynamics of IPS has been studied mainly by multiphoton photoemission induced by a sequence of *direct* electronic transitions from the initial state to the final state, allowing to understand charge localization and electron dynamics processes at solid surfaces [25]. On the other hand, indirect excitations, in which the intermediate IPS state is populated by scattering and relaxation of "hot" electrons, open the possibility of studying population of the intermediate states via scattering assisted processes and to test the current solid state theories involving many-body interactions [25].

This chapter reports the first experimental evidence of multiphoton electron photoemission from the Ag(100) where IPS are detected either with *p*-polarized light (electric field parallel to the plane of incidence) and *s*-polarized light (electric field normal to the plane of incidence). The latter is a process forbidden by the polarization selection rules [16, 26]. The violation of the dipole transition selection rules is consistent with the presence of a hot electron gas generated in the non-linear absorption process, resulting in an indirect, scattering mediated multiphoton photoemission.

A systematic study of this mechanism will be of paramount importance to properly address the theoretical investigations concerning the inelastic lifetime of electrons in metals. In particular, the lifetime of IPS on Ag(100) is determined by electron-electron many body interactions with electrons in the Fermi sea through a dynamically screened potential [24]. This experiment indicates that the presence of a hot electron gas induced by the laser absorption must be considered in the interaction potential. In fact, another interesting novelty of our work is that the effective mass of the IPS excited by indirect multiphoton photoemission is about 6% lower with respect to the free electron mass value measured by direct one-photon population, two-photon photoemission via n=1 IPS [17].

## 4.2 Description of the experimental set-up

The photoemission measurements are performed on a Ag single-crystal oriented along the (100) surface with an error of $\pm 2^\circ$. The surface is polished with standard optical methods to a mirror finish. The light source is an amplified Ti:Sapphire laser system emitting linearly polarized pulses centered at 800 nm with a time width of 150 fs at 1 kHz repetition rate. The UV pulses for single-photon measurements at $h\nu = 6.28$ eV are obtained by quadrupling the Ti:Sapphire fundamental radiation. A work function $\Phi = 4.3 \pm 0.1$ eV is obtained from these measurements. The multiphoton indirect excitation of the IPS is performed with the second harmonic of the fundamental, at a photon energy $h\nu = 3.14$ eV. 2PPE direct excitation of the IPS is accomplished with a traveling-wave optical parametric generator (TOPG) based on parametric interaction in a beta-barium-borate non-linear crystal, pumped by the fundamental of the Ti:Sapphire laser system. The fourth harmonic of the TOPG spans a photon energy range between 3.3 eV and 4.4 eV. The experiments are carried out in a ultrahigh vacuum (UHV) chamber system with a base pressure of $2 \times 10^{-10}$ mbar at room temperature. The sample surface is cleaned by cycles of $Ar^+$ sputtering and subsequent annealing at 400 K. The surface quality is tested with low-energy electron diffraction (LEED) analysis. However, a bright and sharp LEED does not guarantee the needed surface standard to perform the experiment. The cleaning procedure should be carried on until the proper work function for Ag(100) is obtained. All the measurements are carried out in normal detection (with respect to the surface plane) of the photoemitted electron, laser excitation is at an angle of incidence of 30°, either in $p$ and $s$ polarization. The photoelectrons are detected by a time of flight (ToF) electron spectrometer [27] with an energy resolution better than 35 meV at 2 eV electron kinetic energy and an angular resolution of $\pm 0.83^\circ$.

## 4.3 Results and discussion

The IPS are revealed by photoemission using linearly polarized, 150 fs pulses at $h\nu$=4.28 eV and $h\nu$=3.14 eV, in $s$ and $p$ polarization. Since the dipole moment of the IPS is perpendicular to the surface, the probability of excitation with $s$ polarized light in the

dipole approximation is zero [16, 26].

For the direct photoemission process at $h\nu$=4.28 eV, a result consistent with the polarization selection rules for IPS is found, as shown in Fig. 4.1(a). This result is in agreement with the large body of existing literature, where direct excitation is used [16, 26, 28] and it is a clear indication that the experimental data are free of possible artifacts. The negligible secondary electron background observed in these spectra for kinetic energies larger than 4.5 eV, leads to the well-known conclusion that only a photon-induced direct population mechanism is responsible for IPS emission, whereas electron scattering plays a negligible role in these processes.

The detection of the IPS populated at $h\nu$=3.14 eV is significantly more difficult and requires an electron spectrometer with a very high signal to noise ratio. In the present experiment the noise in the detection apparatus (i.e. counts without laser excitation) is negligible (less than $10^{-4}$ counts/s). These spectra are presented in Fig. 4.1(b). The sharp edge observed at about 2 eV kinetic energy fits very well with a room temperature Fermi-Dirac distribution function, up to the point where a high kinetic energy electron tail departs from the low-intensity edge region. In addition, assuming a work-function of 4.3 eV, its kinetic energy is in agreement with a 2PPE photoemission from the Fermi edge. Therefore, this sharp edge can be unambiguously assigned to the Ag(100) Fermi edge resulting from a coherent 2PPE absorption process, while a distinct spectral feature,is detected at 2.76 eV kinetic energy. Interestingly, this feature sits on a high energy secondary electron background that follows closely a Maxwell-Boltzmann like distribution and its intensity is two decades smaller than the emission at the Fermi edge, while its binding energy [1] (BE), determined from work function measurements and the kinetic energy, is 500 meV, in agreement with the BE of n=1 IPS [16, 17]. In addition, the peak of this feature shifts with photon energy by an equal amount. Therefore, it is assigned to a single-photon photoemission from the n=1 IPS.

Rather surprisingly, this spectral feature is still observable with *s* polarized light. This is at variance with measurement using a photon energy of 4.28 eV (see Fig. 4.1(a)), where a total quenching of the IPS electron intensity is observed in *s* polarization. These findings imply that the polarization selection rules, for the population and/or photoemission from

[1] the binding energy is measured with respect to the vacuum level

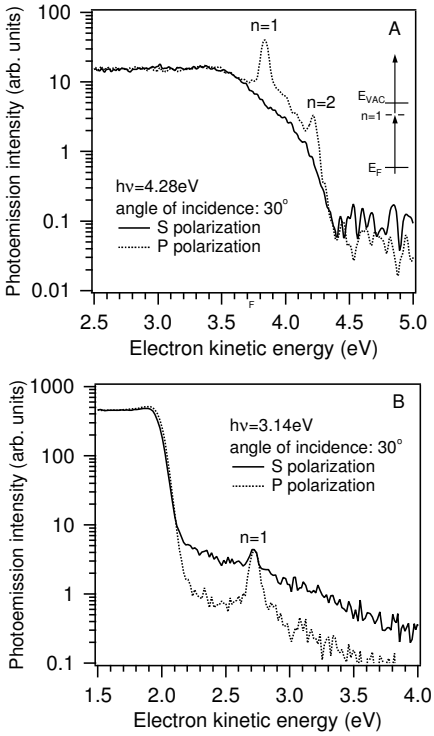


FIGURE 4.1: Multi-photon photoemission spectra from Ag(100) obtained with 150 fs laser pulses at an angle of incidence of 30° with respect to the surface normal. A) Photoemission spectra at $h\nu = 4.28$ eV in $s$ and $p$ polarization. The inset represent a schematic energy level diagrams at $k_{\|} = 0$ of Ag(100) surface states, showing a direct one-photon population, two-photon photoemission via the n=1 IPS. B) Photoemission spectra at $h\nu = 3.14$ eV in $s$ and $p$ polarization. A two-photon population is forbidden by dipole selection rules in $s$ polarization, hence a indirect mechanism must be invoked.

IPS, are violated in $s$ polarization photoemission at $h\nu$=3.14 eV.

To strengthen this claim, the spectral weight of the IPS was measured, at both photon energies, as a function of the angle between the incoming linearly polarized electric

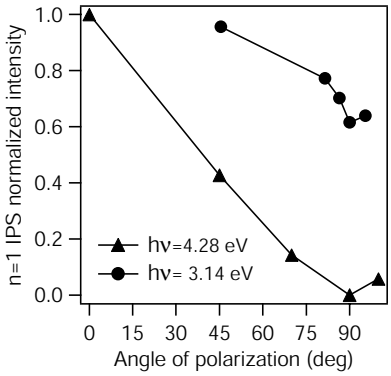


FIGURE 4.2: Dependence of the multiphoton excitation signal of the n=1 image-potential state on the polarization angle. The angle is between the plane of incidence and the electric field vector.

field vector and the plane of incidence (Fig. 4.2). The spectra have the same count rate for the secondary photoelectrons at low kinetic energy. The secondary electrons originate from photo-absorption in the bulk, followed by inelastic scattering and relaxation processes. With this normalization, assuming that substrate absorption is proportional to the secondary electron intensity, we obtain a constant absorbed intensity as the polarization is changed. Any remaining polarization dependence in the spectra is attributed to the difference in excitation mechanism, i.e. direct versus indirect or scattering mediated photoemission, as described in Ref. [25]. The excitation fluences in $p$ polarizations are 0.3 mJ/cm$^2$ at $h\nu$=3.14 eV and 0.03 mJ/cm$^2$ at $h\nu$=4.28 eV. In $s$ polarization the laser fluences are approximately doubled to have the same count rate on the secondary electron emission. In this regime, the production of high-order-harmonics at the surface can not be responsible for high-energy electron photoemission [29]. Fig. 4.2 shows that the intensity of the peak emission is, at most, halved moving from $p$ to $s$ polarization at $h\nu$=3.14 eV, while it goes below the detection limit at $h\nu$=4.28 eV.

To further support the assignment of the spectral feature excited with $s$-polarized light at $h\nu$=3.14 eV to the n=1 IPS, angle resolved photoemission measurements are performed. These measurements are reported in Fig. 4.3, where the dispersion of the IPS peak is shown.

A parabolic dependence of the electron kinetic energy on parallel momentum is clearly detected. The resulting effective electron mass is $m^*/m = 0.91 \pm 0.04$ (see Fig. 4.3(b)). This value is about 6% lower with respect to previously measured n=1 IPS effective mass using direct excitation [17]. Similar results are obtained for excitation with *p*-polarized light.

Among the possible origins of the photoemission from IPS with *s* polarized light, sample roughness should be ruled-out, since it must affect also direct excitations at $h\nu$=4.28 eV. Provided that the photoemission from IPS in *s* polarization is not caused by artifacts, a proper momentum conservation for the photoemission process must be invoked.

The momentum conservation could be rationalized on the base of the following phenomenological model. The photoemission from IPS in metals is a four-step process, 1-absorption of the radiation in the bulk, 2-scattering assisted population of the empty IPS, 3-absorption of the radiation by the IPS electron population, 4-emission of the electron from the populated IPS. When the metal absorbs *s*-polarized photons with energy $h\nu = 3.14$ eV (first step) the IPS can be populated through scattering assisted mechanisms (second step), after single- or multiphoton absorption. The simultaneous presence of the light pulse (150 fs), the populated IPS (lifetime of about 40 fs [26]) and the hot electron gas, which provides the required momentum exchange, may result in a normally forbidden dipole absorption from the IPS state (third step), followed by the electron photoemission above the vacuum level (fourth step). In this frame, it is important to point out that the scattering between the hot electron gas and the population of the IPS is a plausible mechanism to explain the momentum conservation, since the IPS are embedded into a secondary electron background that extends up to 4-4.5 eV (see Fig. 4.1a and Fig. 4.3a). This mechanism is supported also by the observation of a change of the value of the electron effective mass measured at $h\nu = 3.14$ eV, which is lower than the electron effective mass measured using direct two-photon photoemission via the n=1 IPS [17] (see Fig. 4.3).

It is also important to rationalize why IPS are not observed in photoemission at $h\nu =$ 4.28 eV in *s* polarization (see Fig. 4.1A), since in principle also in this case the IPS could be populated from a hot electron gas and hence emitted as in the indirect case at $h\nu = 3.14$ eV. These findings are consistent with the fact that exciting the Ag with photons at 4.28 eV, direct interband transitions from the Ag 4d bands to the bands above the Fermi level

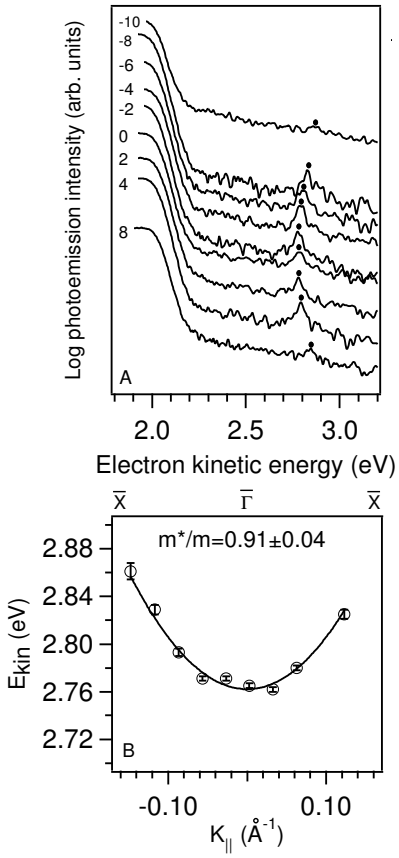


FIGURE 4.3: a) Angular dispersion of the spectral feature appearing on the high-energy electron tail along the $\bar{\Gamma}\bar{X}$ direction of the surface Brillouin zone. Each spectrum is labeled with the detection angle between the Tof axis and the surface normal. The center of each feature is indicated with a dot as a guide to the eye. b) Kinetic energy versus parallel wave-vector dispersion for the peak of the feature. A parabolic fitting gives an effective mass $m^*/m = 0.91 \pm 0.04$.

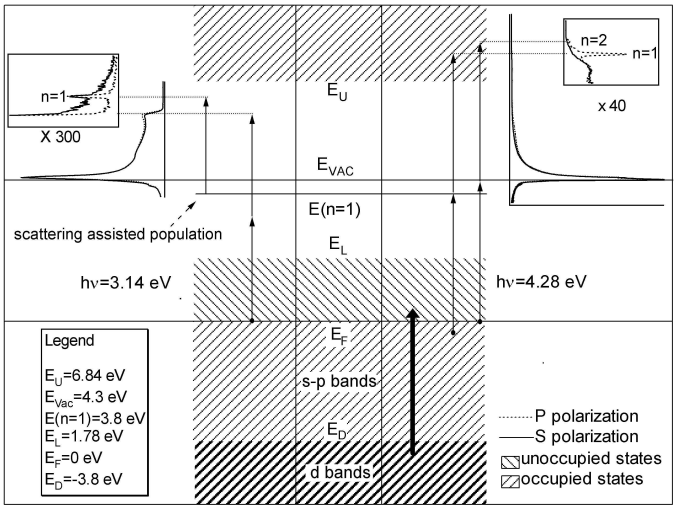


FIGURE 4.4: Schematic potential diagram for an image-potential surface state (n=1) on Ag(100) at $k_{\|} = 0$. A representation of the photoemission processes induced at a photon energy of 3.14 eV and 4.28 eV are shown. The values reported in the legend are from Ref. [31].

(see Fig. 4.4) results in a strong dipole-allowed linear optical absorption (that account for $\sim$ 90% of the absorbed intensity [30, 26]) that prevents the formation of a high-density hot-electron population. On the contrary, such a strong linear interband absorption is not possible with 3.14 eV photon and bulk intraband photoabsorption creates the hot electron gas necessary for the scattering assisted population of the IPS. In agreement with our observations, it has been demonstrated that for direct one-photon population, two-photon photoemission from IPS in bichromatic experiments, the IPS can be observed only for a *p*-*p* combination of pump and probe polarizations. For the *s*-*p* combination the IPSs are not observed as well as for the *s*-*s* and *p*-*s* combinations [16, 26, 28, 25]. This suggests that the hot electron gas is not created exciting the sample with a pump inducing a direct one-photon transition.

To substantiate in a more quantitative way this picture, the excitation fluences are

chosen so that the absorbed number of photons per unit volume is similar (varying in the range 2–7 $10^{19}$ cm$^{-3}$) for both photon energies and polarizations. In Fig. 4.4 the spectra measured at $h\nu = 3.14$ eV and $h\nu = 4.28$ eV, represented on a linear scale, are shown for both *s*- and *p*-polarization. The prominent features in these spectra are the emission near zero kinetic energy, i.e. those originating from the indirect secondary electron emission. However, at $h\nu$=3.14 eV the zero-energy peak vs Fermi edge ratio is lower with respect to that measured at $h\nu$=4.28 eV. This confirms the role of the direct interband absorption from the d bands at 4.28 eV, that populate the available states near the Fermi level, giving an additional contribution to the zero-energy peak intensity. These results demonstrate that the rate of electron-electron scattering and its influence on photoemission can be controlled choosing different wavelengths and polarizations.

The formation of non-equilibrium electrons in noble metals and the electron-electron scattering rate is a matter of intensive discussion. The present experiment shows that the role of indirect transitions and the associated electron scattering mechanisms has not been fully considered yet. In particular, the experimental evidence that IPS can be observed in multiphoton photoemission processes either with *p*- and *s*-polarized light can be regarded as a step toward controlling the behavior of electronic states in a solid populated via scattering process and as a set of important experiments to test the current theories involving many-body electron interactions.

## 4.4 Conclusions

In conclusion, the novelty of the work presented in this chapter is the experimental evidence of multiphoton electron photoemission from the Ag(100), detected either with *p*- and *s*-polarized light. The latter is a transition forbidden by the polarization selection rules. The violation of these rules is consistent with an interaction between the hot electron gas, generated in the non-linear absorption process, and the electrons in the IPS . The presence of this interaction is strengthened by the measure of the IPS electron effective mass of 0.91 in free electron mass units, i.e. 6% less of the effective electron mass measured by direct one-photon population, two-photon photoemission.

# Chapter 5

# Evidence of above-threshold photoemission in Ag(100)

Nonlinear photoemission from a silver monocrystal is investigated with femtosecond laser pulses. Clear and unambiguous evidence of non-resonant three photon above-threshold photoionization in solids is reported for the first time. Three independent experimental evidences are provided. Two and three photon Fermi edges are separated by one photon energy and well fitted by a Fermi-Dirac distribution with the same parameters. Integrated electron yield measurements show the correct scaling law with laser intensity. Upon an energy shift $h\Delta\nu$ of the photon energy, the three-photon Fermi edge is energy shifted by an amount $3h\Delta\nu$.

## 5.1 Motivation

In recent years a significant effort has been dedicated to the study of above-threshold ionization (ATI)[32, 33, 34, 35, 36]. ATI is the process by which an atom, subject to an intense electromagnetic field of frequency $\nu$, is ionized by the absorption of a number of

photons that exceeds the minimum number strictly necessary to overcome the ionization potential $W_{ion}$. Perturbation theory predicts that the photoemitted electron spectrum should consist of emissions located at energies

$$E_n = nh\nu - W_{ion}. \tag{5.1}$$

where $n$ is equal to or greater than the minimum number of photons necessary for ionization.

The phenomenon has been clearly observed in atoms [32, 33, 34, 35] and molecules [36], while its equivalent in solids, referred as above threshold photoionization (ATP), lacks of the experimental evidences otherwise present. Actually a few studies do claim observations of ATP in solids [37, 38, 39], but none of them shows spectra were above-threshold multiphoton replica of the Fermi edge are clearly visible and unambiguously identified.

Striking and unambiguous observation of a three photon above-threshold photoemission at the Ag(100) surface is here reported.

Recognition of an above threshold Fermi-edge should rely on several independent validations. Indeed, by exciting the sample with a photon at an energy $h\nu = 3.14$ eV, a two-photon edge and an above threshold three-photon edge, resulting from a one-photon replica of the two-photon edge, are observed. The two- and three-photon emissions are fitted by the same Fermi-Dirac (FD) distribution function [1]. This fact allows to identify these features as a two- and three-photon replica of the Fermi edge respectively. Furthermore, total photoemission yield measurements show a quadratic and cubic dependence on laser intensity of the two and three-photon Fermi edges. This measurement endorses the photoemission of the above-threshold Fermi edge as third order process. A last experimental evidence resides in an energy shift of the above mentioned features by an amount of 160 meV and 240 meV respectively, upon a photon energy shift of 80 meV. This measurement can be regarded as a conclusive proof that the two Fermi edges are photoemitted by two- and three-photon processes.

[1] The fit was performed both with a Fermi-Dirac distribution and a Fermi-Dirac distribution multiplied by a free-electron gas density of states. No significant difference could be appreciated

## 5.2 Description of the experimental set-up

The experimental parameters have been tailored in order to ensure a perturbative regime and to avoid spatial charge effects that could hinder the observation of a multi-photon Fermi-edge. In this frame, an important fator, in the present experiment, is the adiabaticity or Keldysh parameter $\gamma$, defined as the ratio of the tunnelling time to the optical period:

$$\gamma = \frac{\omega}{e}\sqrt{\frac{mc\epsilon_0 W_b}{I}}, \tag{5.2}$$

where $m$ is the electron rest mass, $e$ is the electron charge, $\epsilon_0$ is the vacuum permittivity, $\omega$ and $I$ are the laser angular frequency and intensity respectively, and $W_b$ is the binding energy of the most weakly bound electron. In the present case $W_b$ coincides with the work function $\Phi$. The Keldysh parameter discriminates among multiphoton-ionization ($\gamma \gg 1$) and tunneling ionization ($\gamma \ll 1$) regimes [40]. A laser pulse intensity $I \sim 0.4$ GW/cm$^2$, at a wavelength of 395 nm, impinging at an angle of incidence of 30°, results, once corrected for Fresnel losses [2], in an absorbed intensity $\sim 60$ MW/cm$^2$. This figure gives a $\gamma \sim 1500$, thus ensuring the experiment to be carried out within the perturbative regime.

Space charge effects are negligible. Measurement performed at different laser intensities, spanning the range 0.1-1 GW/cm$^2$, show a modest modifications in the spectra. To maximize the photoemission electron yield and reduce spectra sampling time, a space-charge induced work function shift of 200 meV, compared to the value obtained from direct photoemission measurements ($h\nu$=6.28), is accepted in the measured non-linear spectra. It is worth mentioning that the emergence of the three-photon Fermi edge from the hot-electron population background required several time consuming data acquisitions. This point can be appreciated comparing the spectra reported in this chapter with the ones reported in a recent work [42]. At this intensity ponderomotive potential is of no concern.

The photoemission measurements are performed on a Ag single-crystal oriented along the (100) surface with an error of $\pm 2\,^\circ$. The light source is an amplified Ti:Sapphire laser system emitting linearly polarized pulses with a time width of 150 fs at 1 kHz repetition rate. The fundamental wavelength can be tuned in the range 780-810 nm, the second harmonic spans the photon energy range 3.06-3.18 eV. The experiments are carried out

[2] The calculation is performed using the index of refraction reported in [41].

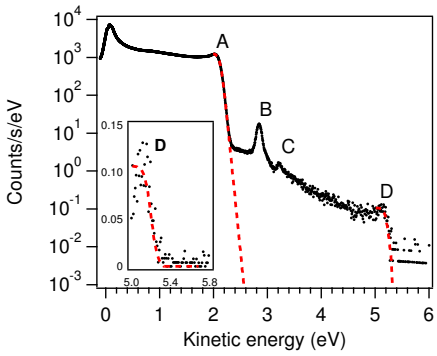


FIGURE 5.1: Photoemission spectrum from Ag(100) obtained with 150 fs-3.14 eV laser pulses in semilog plot. The light is p-polarized and its angle of incidence is 30° with respect to the surface normal. The dashed lines (figure and inset) are a Fermi-Dirac fit at a temperature of 348 K. A temperature slightly in excess of 300 K can be ascribed to the modest space-charge deformation of the Fermi-edge. Letters A and D label the 2-photon and the 3-photon Fermi edges respectively. The 3-photon Fermi edge is reported in the inset in linear scale. Letters B and C identify the first two image states.

in a ultrahigh vacuum (UHV) chamber system with a base pressure of $2 \times 10^{-10}$ mbar at room temperature. All the measurements are carried out in normal detection (with respect to the surface plane) of the photoemitted electron and excitation at an angle of incidence of 30° in both $p$ and $s$ polarization. Details of the experimental set-up and sample preparation are reported in previous chapters.

## 5.3 Results and discussion

### 5.3.1 *Three-photon above-threshold Fermi edge*

The spectrum, obtained irradiating with photons of energy $h\nu = 3.14$ eV, is shown in Fig. 5.1. Two distinct portions of the spectrum are clearly distinguishable. The first one lays in the energy range below 2.3 eV. The second one lays in the energy range between 2.3 eV and 5.3 eV. The first portion of the spectrum is attributed to a direct two-photon

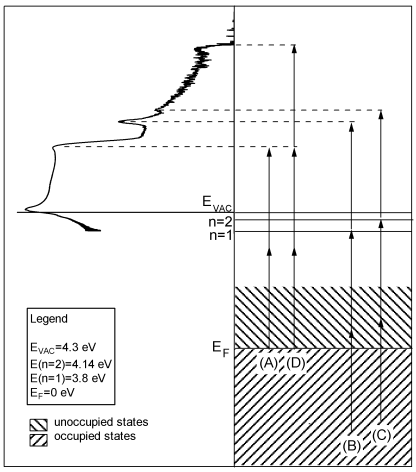


FIGURE 5.2: Schematic energy diagram for Ag(100) at the Γ point and photoemission processes involved in the measured spectrum. The values reported in the legend are from Ref.[31]. Labels A, B, C and D are defined as in the text.

photoemission process that involves electrons occupying the s-p bands lying just below the Fermi energy, whereas the second portion resembles, disregarding peaks B and D on which I will comment shortly, the low energy portion upon translation of one photon energy. This evidence is particularly clear when considering the steps labelled A and D in the photoemission spectrum. Step A is recognized as the two-photon Fermi edge, in fact $E_A = 2h\nu - \Phi$ and the spectrum is well fitted by a Fermi-Dirac function at 348 K. Step D is energy shifted by a photon energy $h\nu$ with respect to step A and it fits a Fermi-Dirac function with the same parameters as the above mentioned one. The fitting temperature slightly in excess of 300 K can be ascribed to the modest space-charge induced broadening of the Fermi edge. Step D is thus identified as a three-photon Fermi edge. The peaks labelled B and C are attributed to the n=1 and n=2 Rydberg-like image potential states (IPS) as a result of a two-step photoemission process. In the first step electrons in the s-p conduction bands populate the IPS both via one photon-resonant two photon ionization [43] process and incoherent two photon ionization. The resonances are provided by the 2

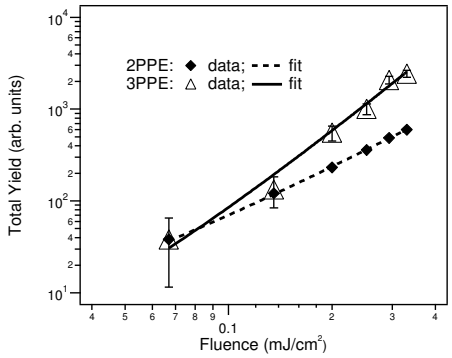


FIGURE 5.3: Integrated electron yield versus laser fluence at a photon energy of 3.14 eV. The empty triangles refer to data obtained integrating the photoemission spectra in the energy range between 0.41 and 2.11 eV; the full triangles refer to data obtained integrating the photoemission spectra in the energy range between 3.55 and 5.25 eV. The latter data are multiplied by a factor of $2.6 \times 10^5$ for ease of visibility. The full and dashed line are polynomial fits indicating a second and third order power dependence on intensity respectively.

eV wide portion of the s-p conduction band lying above the Fermi level. In the second step these electrons are then photoemitted from the IPS via the absorption of a third photon. The measured binding energies are consistent with the expected theoretical values [44] and in good agreement with recent experimental findings [17]. The present discussion is schematically illustrated in Fig. 5.2

### 5.3.2 *Integrated electron yield measurements*

To further support this interpretation, the integrated electron yields were measured at different laser intensities. The results are reported in Fig. 5.3. The integrated yield in the energy range between 0.41 and 2.11 eV scales as $I^2$, whereas the integrated yield in the energy range between 3.55 and 5.25 eV scales as $I^3$. The integrations on the Fermi distribution-like portions of the spectrum have been performed on energy ranges shifted by one photon energy with respect to each other. These findings are consistent with a

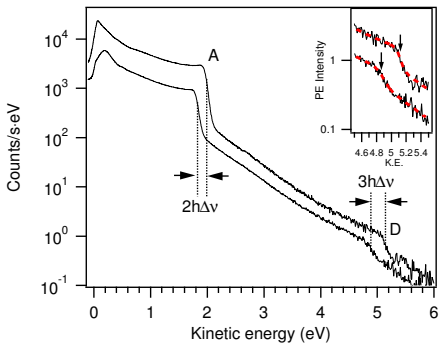


FIGURE 5.4: Photoemission spectra from Ag(100) obtained with 150 fs s-polarized laser pulses at $h\nu = 3.14$ eV (upper curve) and $h\nu = 3.06$ eV (lower curve) in semilog plot. The angle of incidence is 30° with respect to the surface normal. The impinging intensity is 0.14 GW/cm$^2$. The plots are displaced vertically for ease of visualization. In the inset the curves, displaced vertically, are shown with a fit obtained from a sum of a Fermi-Dirac and a Maxwell-Boltzmann function convoluted with a gaussian function.

second and third-order photoemission of the Fermi edge.

### 5.3.3 *Frequency shift measurements*

A conclusive proof is the measurement of the energy shift in kinetic energy of the two and three-photon Fermi edges upon a frequency shift of $h\Delta\nu$=80 meV of the impinging radiation (see Eq. 5.1). Shifting the central laser photon energy from 3.14 eV to 3.06 eV, we observe an energy shift of the edges A and D of the spectrum by an amount of $2h\Delta\nu$=160 meV and $3h\Delta\nu$=240 meV respectively, implying that edges A and D are emitted by a two and three-photon process respectivelys shown in Fig. 5.4

## 5.4 Free-free electron transition

The experimental evidences provided so far validate an interpretation of the phenomenon within the frame of time-dependent perturbation theory [43]. Only the second- and third-

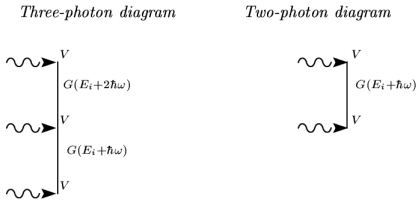


FIGURE 5.5: Feynman diagrams associated to the second and third order photoemission. The diagrams are read upward and constitute a pictorial representation of the transition matrix elements.

order perturbative contribution to the two and three-photon processes respectively (see Fig. 5.5) are considered, while higher order diagrams are negligible. The eigenvalue problem for the unperturbed semi-infinite crystal hamiltonian

$$\widehat{H}_0 \left|j\right\rangle = E_j \left|j\right\rangle \tag{5.3}$$

comprises eigenvalues both in the discrete and continuum spectrum; the interaction Hamiltonian in the *velocity gauge* is

$$V = \frac{ie}{2m\omega} E^* p \ + \ c.c, \tag{5.4}$$

with $p = \epsilon \cdot \mathbf{p}$, $\epsilon$ being the polarization unit vector of the e.m field $\mathbf{E}$ and $\mathbf{p}$ the momentum operator, is treated as a perturbation. The differential cross-section for an n-photon absorption involving the initial and final states $|i\rangle$ and $|f\rangle$ is,

$$\frac{dW^{(n)}_{i\to f}(\mathbf{k}_f)}{d\Omega} = \frac{2\pi}{\hbar^2}\left(\frac{e^2}{2m^2 c\epsilon_0}\frac{I}{\omega^2}\right)^n \left|T^{(n)}_{i\to f}(\mathbf{k}_f)\right|^2 \rho(E_{k_f}), \tag{5.5}$$

where $\epsilon_0$ is the electric permittivity, $e$ the electron charge, $\rho\left(E_{k_f}\right)$ the free electron final density of states evaluated at the photoemitted electron energy $E_{k_f} = nh\nu - \Phi$, $\mathbf{k_f}$ being the wave vector of the electron in the final state, whose modulus is determined from energy conservation $\hbar^2 k_f^2/2m = n\hbar\omega - \Phi$. $I$ is the *absorbed* laser intensity. The transition matrix element remains defined as

$$T_{i\to f}^{(n)} \equiv \langle f|\, p \underbrace{G\left(E_i + (n-1)\,\hbar\omega\right) p}_{n-1\ such\ terms} ... G\left(E_i + \hbar\omega\right) p\, |i\rangle \tag{5.6}$$

where $p$ is reminiscent of the photon-electron interaction and $G\left(E_i + m\hbar\omega\right)$ is the propagator of the unperturbed hamiltonian after absorption of the $m^{th}$ photon

$$G\left(E_i + m\hbar\omega\right) = \sum\!\!\!\!\!\!\int_j \frac{|j\rangle\langle j|}{(E_i + m\hbar\omega) - E_j}, \tag{5.7}$$

$E_i$ being the energy of the initial state.

Since the pioneering work of Agostini et al. [32] on ATI in atoms, the absorption of additional photons beyond the ionization threshold has often been modelled as a two step process where the electron is ionized by the minimum number of necessary light quanta and it absorbs the extra photons once above threshold. The naive term 'free-free transition' was coined to define this last step (see third photon involved in process (D) of Fig. 5.2). The before mentioned transition has null matrix element and several authors invoked a modification of the potential felt by the electron, once above threshold, or the interaction of the freed electron with ponderomotive forces to solve the discrepancy [32, 33, 45].

I argue that, within the frame of non-resonant coherent perturbation theory, the so called 'free-free' transition actually involves the mixing of the final free electron state with *all* the unperturbed hamiltonian eigenstates (see Eq. 5.6 and Eq. 5.7) and not only with the eigenstates entering the continuum spectrum, that would give null matrix elements. Experimentally, it is found that the ratio $\partial_\Omega W_{i\to f}^{(3)}\left(\mathbf{k}_f\right) / \partial_\Omega W_{i\to f}^{(2)}\left(\mathbf{k}_f\right)$ among the 3-photon and the 2-photon differential cross-sections $\sim 10^{-4}$. A theoretical estimate for the above mentioned ratio gives a value two orders of magnitude lower. The calculation was carried out neglecting the details of the matrix elements, within the same approximations used in [43]:

$$\frac{T_{i\to f}^{(3)}\left(\mathbf{k}_f\right)}{T_{i\to f}^{(2)}\left(\mathbf{k}_f\right)} \approx \sum\!\!\!\!\!\!\int_j \frac{p}{(E_i - E_j) + 2\hbar\omega}, \tag{5.8}$$

$p \sim \hbar k_f = \sqrt{2m(3\hbar\omega - \Phi)}$. Assuming that only one particular eigenvalue $E_j = \tilde{E}$ is relevant in the sum, the right term in Eq. 5.8 reduces to $p/\left(\Delta E + 2\hbar\omega\right)$, where $\Delta E \equiv$

$E_i - \tilde{E}$. I focused on the values of $\Delta E$ that fall in the interval $[-1.78, 0]$ eV and $[-3.8, -4.3]$ eV, the former range meaning that the prevailing unperturbed eigenstates contributing to the transition matrix are the unoccupied s-p bulk states laying 2 eV above the Fermi level, the latter privileges image-states lying below the vacuum level (refer to Fig. 5.2). Note that it never occurs $\Delta E + 2\hbar\omega = 0$, being the emission process *non*-resonant. The discrepancy among the experimental data and the crude estimate here discussed is comparable with the discrepancies reported in the literature when applying much more involved calculations [43]. This discrepancy is still an open issue.

## 5.5 Conclusions

In conclusion, for the first time unambiguous evidence of an above threshold photoemitted Fermi edge in solids is here reported. Three distinct and independent experimental proofs are provided. Two and three photon Fermi edges are separated by one photon energy and well fitted by the same Fermi-Dirac distribution. Integrated electron yield measurements show the proper scaling law with laser intensity. Upon an energy shift $h\Delta\nu$ of the photon energy, the three-photon Fermi edge is energy shifted by an amount $3h\Delta\nu$.

# Chapter 6

# Design of a multiple ring Aharonov-Bohm gradiometer

A novel semiconductor structure, serving as a nanometer-sized gradiometer, is proposed. The device relies on four concatenated Aharonov-Bohm rings, three of them lying on mutually perpendicular planes. Conductance oscillations, due to magnetically induced electron wavefunction phase shift, allow to access information on the concatenated magnetic field with respect to all the device's planes. Feasibility of the device fabrication and potential applications are discussed.

## 6.1 Motivation

The quantum mechanical phase of an electron wavefunction can be controlled by means of electromagnetic potentials, as predicted by Aharonov and Bohm in their 1958 seminal work [46]. A charged particle wavefunction in presence of an electromagnetic potential $A_\mu$, even in absence of the electromagnetic fields, experiences a phase shift $\propto \int_\Gamma A_\mu dx^\mu$, with $\Gamma$ describing the particle's path and where the 4-vectors position and potential and

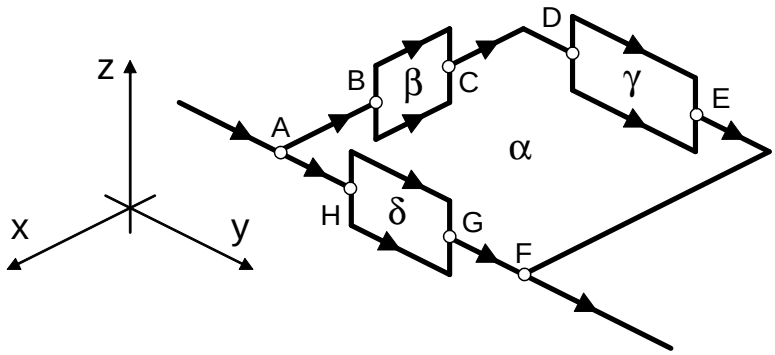


FIGURE 6.1: Device geometry. The four concatenated anula constituting the device are labeled $\alpha, \beta, \gamma, \delta$. Arrows indicate electron propagation path from source to drain.

their scalar product have been written following Einstein notation. This shift can produce observable effects when interference between different paths is involved in the propagation of the particle. This theory has highlighted the central role of potentials with respect to forces in quantum mechanics and has also provided a theoretical basis for some electronic quantum interference devices, such as Aharonov-Bohm (AB) rings. Progress in growth and nanofabrication technologies allows nowadays to exploit AB effects in semiconductor heterostructures [8, 9, 47, 48, 49, 50] for the realization of coherent nano-device prototypes.

In this chapter I propose a novel device concept relying on multiple concatenated AB rings, three of them lying on mutually perpendicular planes (see Fig. 6.1). Multiple conductance oscillations are expected as a consequence of the varying magnetic field concatenated to the various ring areas. The analysis of these oscillations allows a direct measurement of the vectorial magnetic field, up to a limited direction uncertainty due to the time-reversal symmetry of the system. I will demonstrate that the proposed device can serve as a nano-scale gradiometer. The most interesting characteristic of the device is that it allows a vectorial measurement of the magnetic field on a very compact volume, that is at the nanometric scale: for this reason it could be a candidate for the realization of a non invasive probe for measuring nano-particles magnetic susceptibility tensors.

## 6.2 Device concept

Consider the device geometry shown in Fig.6.1. A single channel model of spinless electrons for the quantum wires constituting the various rings is adopted. This model can be applied to a device where the wires are so narrow that only a few 1D channels are involved in the transmission.

At cryogenic temperatures, provided a coherence-length greater than the device dimensions, the conductance $G$ follows $G = 2e^2T/h$ [11], with $e$ the modulus of the electron charge, $h$ the Planck constant and $T$ the transmission coefficient at the Fermi energy. I now address the problem of calculating the transmission coefficient $T$, assuming an external magnetic field $\mathbf{B}$ is present (see Fig. 6.1). The electromagnetic field configuration is described in a gauge where the scalar potential vanishes, with $\mathbf{B} = \nabla \times \mathbf{A}$, $\mathbf{A}$ being the vector potential. Neglecting multiple reflections [1], the total transmission amplitude through a simple ring can be calculated summing the amplitudes for the two possible paths

$$t = t_\uparrow P_\uparrow t'_\uparrow + t_\downarrow P_\downarrow t'_\downarrow. \tag{6.1}$$

Here $t_\uparrow$, $t_\downarrow$ (see Fig. 6.2) are the transmission amplitudes from the left lead to the upper and lower branch respectively, $t'_\uparrow$, $t'_\downarrow$ are the transmission amplitudes from the upper and lower branch respectively to the right lead, while $P_\uparrow$ and $P_\downarrow$ take into account the phase shift aquired by the electron wavefunction while propagating through the upper and lower branch respectively. I assume the magnetic field only affects the phase following the relation

$$P_i(B) = P_i(0) \exp\left[ i \frac{e}{\hbar} \int_{\Gamma_i} \mathbf{A}\mathbf{dr} \right] \qquad i = \uparrow, \downarrow \tag{6.2}$$

[1] In the experiment AB oscillations are detected due to the interference of the electron encircling the device. Oscillations should be observed as peaks in the Fourier spectra of the magneto-conductance at multiples $ne/h$ of the fundamentals A-B frequencies $\omega_\alpha$, $\omega_\beta$, $\omega_\gamma$, $\omega_\delta$ and at their linear combinations, where $n$ is the number of times a ring has been encircled. Note that this number can differ from ring to ring: the longer the rings arms the lower the chances of it to be encircled more than ones, this being due to phase-breaking scattering events. The amplitude of a $h/ne$ oscillation strength scales as $\exp(-nL/L_\phi)$, where $L$ is the path length and the coherence length $L_\phi \propto 1/T$ [51]. These argumentations, together with the relatively long branches involved, justify neglecting multiple reflections.

where $\Gamma_i$ is the path the electron follows in branch $i$. In the following I will also use the notation $P_{ij}$ to indicate the phase shift for an electron propagating from point $i$ to point $j$. I will assume, for sake of simplicity, that the transmission coefficients at the branching points are equal, i.e. $t_{i\uparrow}$=$t_{i\downarrow}$ and $t'_{i\uparrow}$=$t'_{i\downarrow}$, where the subscript i indicates the ring the transmission amplitude refers to. The complete device structure is now considered (refer to Fig. 6.1 for details). The total transmission amplitude is

$$t_\alpha = t_{\alpha\downarrow} P_{AB} t_\beta P_{CD} t_\gamma P_{EF} t'_{\alpha\downarrow} + t_{\alpha\uparrow} P_{AH} t_\delta P_{GF} t'_{\alpha\uparrow}. \tag{6.3}$$

Here $t_\beta$, $t_\gamma$ and $t_\delta$ are the transmission amplitudes through rings $\beta$, $\gamma$ and $\delta$. I define the following coefficients

$$\begin{aligned} t_{AF\downarrow} &= t_{\alpha\downarrow} t_{\beta\uparrow} t'_{\beta\uparrow} t_{\gamma\uparrow} t'_{\gamma\uparrow} t'_{\alpha\downarrow} \\ t_{AF\uparrow} &= t_{\alpha\uparrow} t_{\delta\uparrow} t'_{\delta\uparrow} t'_{\alpha\uparrow}. \end{aligned}$$

Performing some algebra the transmission coefficent $|t_\alpha|^2$ is calculated obtaining

$$\begin{aligned} T &= 16|t_{AF\downarrow}|^2 \prod_{\beta,\gamma} \cos^2\left[\pi \frac{\Phi_i(\mathbf{B})}{\Phi_0}\right] \\ &+ 4|t_{AF\uparrow}|^2 \cos^2\left[\pi \frac{\Phi_\delta(\mathbf{B})}{\Phi_0}\right] \\ &+ 16|t_{AF\downarrow}||t_{AF\uparrow}| \cos\left[2\pi \frac{\Phi_\alpha(\mathbf{B})}{\Phi_0} + \varphi\right] \\ &\times \prod_{\beta,\gamma,\delta} \cos\left[\pi \frac{\Phi_i(\mathbf{B})}{\Phi_0}\right]. \end{aligned} \tag{6.4}$$

Here $\Phi_0$ is the flux quantum $h/e$, $\Phi_i(\mathbf{B})$ is the flux of $\mathbf{B}$ through ring $i$, and $\varphi$ is a phase factor taking into account the asymmetry in ring $\alpha$. Due to time-reversal symmetry, in a two terminal configuration $\varphi$ can only acquire values 0 or $\pi$ [52]. As the rings in a real device are very small it is convenient to write the magnetic flux as $\Phi_i(\mathbf{B}) = \mathbf{S}_i\mathbf{B}$, where $\mathbf{S}_i = S_i\mathbf{n}_i$ with $S_i$ as ring $i$ surface area and $\mathbf{n}_i$ the surface unit vector. The first two terms in equation (6.4) are the contributions due to the paths $AF\downarrow$ and $AF\uparrow$ considered alone.

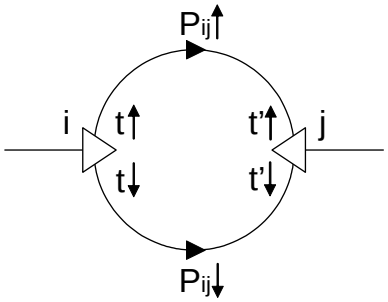


FIGURE 6.2: Subscripts ij indicate the path extremes. $P_\uparrow$ and $P_\downarrow$ describe propagation along the upper and the lower branch respectively. Triangles denote branching points, formally treated as scattering centers. The transmission amplitudes $t_\uparrow$, $t'_\uparrow$ refer to scattering events that involve the upper branch whereas $t_\downarrow$ and $t'_\downarrow$ refer to scattering events involving the lower branch. Primed transmission amplitudes refer to scattering events leading out of the ring geometry whereas unprimed ones denote scattering events leading into the ring geometry. The upper (lower) branch develops in the plane x>0 (x<0) in ring $\alpha$ and in the plane z>0 (z<0) in rings $\beta$, $\delta$, $\gamma$. Refer to Fig. 6.1 for the device geometry.

Each ring contributes a factor $\cos^2(\pi\Phi_i(\mathbf{B})/\Phi_0)$, and in particular transmission of the two rings in series on branch $AF\downarrow$ is the product of the rings individual transmissions. The last term is the interference term among paths $AF\downarrow$ and $AF\uparrow$.

It is useful to analyze the frequencies of the oscillations in $\mathbf{B}$ of the transmission coefficient as the measurement of these frequencies allows in fact to reconstruct the magnetic field direction. A list of the oscillation frequencies, obtained developing equation (6.4), is reported in Table 6.1. Thirteen different oscillating terms appear in the expression for the transmission coefficient. Only four frequencies can be considered as independent, a set of nine linear equations relating the entire ensemble of thirteen. We expressed all of them in terms of the four fundamental frequencies $\omega_i$ with $i = \alpha, \beta, \gamma, \delta$ arising from the four AB rings. These frequencies are related to the magnetic field by

$$\omega_i = \frac{2\pi}{\Phi_0}\frac{d\Phi_i(\mathbf{B})}{dB}. \tag{6.5}$$

| | Frequencies (Tesla$^{-1}$) |
|---|---|
| 1 | $\omega_\beta$ |
| 2 | $\omega_\gamma$ |
| 3 | $\omega_\delta$ |
| 4-5 | $\omega_\beta \pm \omega_\gamma$ |
| 6-13 | $\omega_\alpha + (\pm\omega_\beta \pm \omega_\gamma \pm \omega_\delta)/2$ |

TABLE 6.1: List of transmission oscillation frequencies obtained developing equation (6.4).

Note that, following the device structure reported in Fig. 6.1, two of the fundamental frequencies, namely $\omega_\gamma$ and $\omega_\delta$ are strictly related. In fact they arise from the interference in two rings lying in parallel planes so that their ratio is fixed:

$$\omega_\gamma/\omega_\delta = S_\gamma/S_\delta. \tag{6.6}$$

The apparent redundance of the two rings $\gamma$ and $\delta$ is indeed necessary to distinguish among oscillations ($\omega_\beta$ and $\omega_\gamma$) resulting from magnetic field variation in the x and y directions. In practice the insertion of ring $\gamma$ brakes the symmetry with respect to the exchange of rings $\beta$ and $\delta$, that otherwise would be present.

We now have all the ingredients to access information about the direction of the applied magnetic field **B**. Sweeping the field, conductance $G$ oscillates and, by performing a Fourier transform of the $G(B)$ data set, one should obtain the frequencies listed in Table 6.1. Following the various relations linking these not-independent frequencies it is possible to extract the four fundamental frequencies $\omega_i$ and finally calculate the magnetic field direction:

$$(\pm\frac{\phi_0}{2\pi}\omega_\gamma S_\gamma^{-1}, \pm\frac{\phi_0}{2\pi}\omega_\beta S_\beta^{-1}, \pm\frac{\phi_0}{2\pi}\omega_\alpha S_\alpha^{-1}). \tag{6.7}$$

Due to time-reversal symmetry this direction is indeed not univocally determined. The experiment can infact only access the absolute value of the frequencies $\omega_i$ as all the transmission coefficients involved are even functions in the concatenated field flux. As a

consequence, no change in the two-terminal conductance is expected upon sign change of one of the components (x, y or z) of the magnetic field. For this reason single conductance measurements cannot allow to distinguish between the $2^3 = 8$ equivalent directions of the magnetic field.

## 6.3 Device proposal

In this section a fabrication strategy is outlined for a prototype of the device. Starting from a GaAs/AlGaAs structure containing a double two dimensional electron gas (2DEG), it is possible to implement both the horizonal and vertical interferometric rings required for the proposed device.

A simulation was made for a 80 nm GaAs quantum well buried 70 nm below the surface and sandwiched between $Al_{0.25}Ga_{0.75}As$ barriers. Two Si $\delta$-doping layers are placed 20 nm (surface side) and 55 nm (substrate side) from the well, doping concentration being in the order of $10^{24}$ m$^{-3}$. The 1D Poisson-Schrödinger equations was solved to calculate the band structure of this heterostructure (see Fig. 6.3).

The peculiarity of this design is the presence of an Hartree barrier due to Coulomb interaction between electrons populating the quantum well. Following simulation results, this "soft" barrier is expected to give rise to two closely spaced subbands below the Fermi energy. This scheme, respect to the usual double quantum well structures, avoids the need for a central $Al_xGa_{1-x}As$ barrier that introduces interface roughness and alloy scattering and degrades electronic mobility [53, 54]. By metal-gating, the structure can be easily tuned on a single or double 2DEG (see Fig.6.3, panel (a)). This characteristic is a clue element for the realization of the various vertical rings.

Ring $\alpha$ can be obtained by standard e-beam lithography and wet etching techniques [55, 56]. The ring's arms should be quantum wires supporting a double 1D channel due to the presence of a double 2DEG structure. Modelling the lateral confining potential of the arms as an hard-wall like potential and assuming [2] a sheet carrier concentration of $5 \times 10^{15}$ m$^{-3}$ a width of 100 nm for the quantum wire allows only two occupied subbands. An experimental study, carried out in $Al_xGa_{1-x}As$ wet etched rings of comparable lateral

[2] The figure results from the numerical solution of the self consistent Poisson-Schrödinger problem.

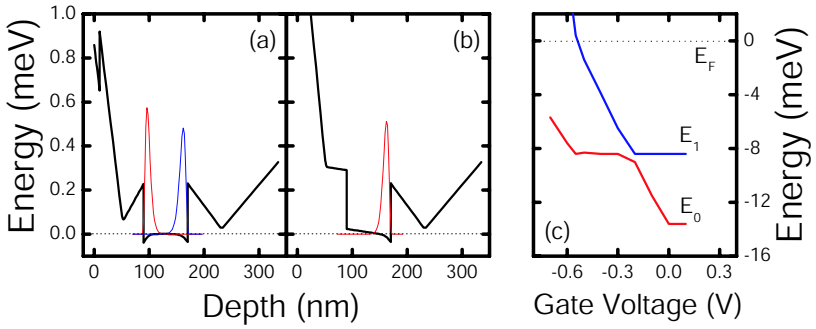


FIGURE 6.3: Conduction-band energy diagrams (solid black line) and charge-density profile of the occupied subbands (solid red line and solid blue line are the charge-density profiles of the subbands of energy $E_0$ and $E_1$ respectively) for unbias situation, Panel (a), and for $V_{bias} = -0.6$, Panel (b). Note that, at $V_{bias} = -0.2$ a cross over occures: the charge density profile related to $E_0$ shifts on the deep side (with respect to the surface) of the quantum well, whereas the charge density profile related to $E_1$ shifts on the shallow side of the quantum well. Panel (c) Subband-bottom energy $E_0$ (red line) and $E_1$ (blue line) referred to the Fermi level $E_F$ as a function of the gate bias. The calculations are performed solving numerically the Poisson-Schrödinger problem at 4.2 K.

size, reported a coherence length at 1 K in excess of 5 $\mu$m [51]. This makes one confident the proposed device is within the required dimensions for coherent transport (see Fig. 6.4 for device's dimensions).

The vertical rings can be obtained by gating the arms to locally control the number of propagating channels. Ungated regions can serve as double channels in parallel, while appropriately biased gated regions constitute single channels (see Fig. 6.3). Rings can be fabricated alternating gated-ungated-gated portions on the arms of the planar ring. Lengths of 500($\beta$), 600($\gamma$) and 400($\delta$) nm are chosen for the ungated regions. The overall device is shown in Fig. 6.4. The surface area enclosed by the various rings is also estimated. Self-consistent calculation of the two subband wavefunctions yields a value of the center-to-center distance $L_z$ among the two paths of about 70 nm (see Fig. 6.3, panel (a)). The following values are expected

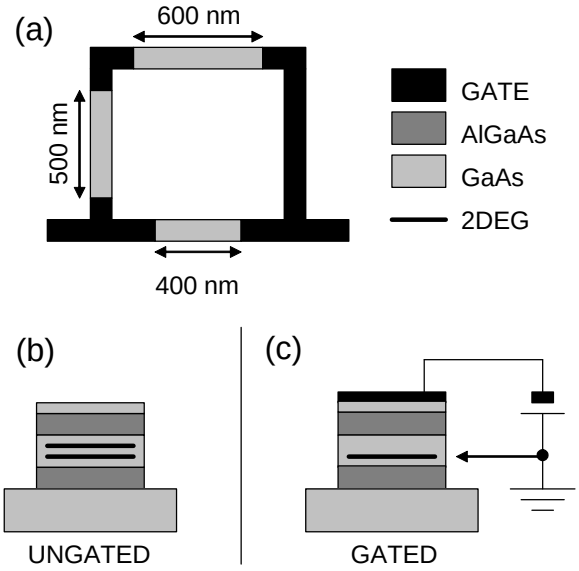


FIGURE 6.4: Panel (a) Top view (xy-plane) of the device: etched ring $\alpha$. The vertical rings lay beneath the *GaAs* regions. Panel (b) and (c): cross section of the device for ungated ((b)) and gated ((c)) regions.

$$S_\alpha \simeq 0.7200\ \mu\mathrm{m}^2 \quad S_\beta \simeq 0.0320\ \mu\mathrm{m}^2$$
$$S_\delta \simeq 0.0256\ \mu\mathrm{m}^2 \quad S_\gamma \simeq 0.0384\ \mu\mathrm{m}^2.$$

It is now demonstrated, through a numerical test, the device at work. A random direction for the magnetic field has been chosen and the conductance together with its Fourier transform have been calculated following equation (6.4) and using the above mentioned values for the device geometry. Conductance data are shown in Fig. 6.5 while detected frequencies are listed in Table 6.2.

The data have been grouped in two sets: group I contains eight frequencies in the range $730 - 810$ Tesla$^{-1}$, group II contains five frequencies an order of magnitude smaller.

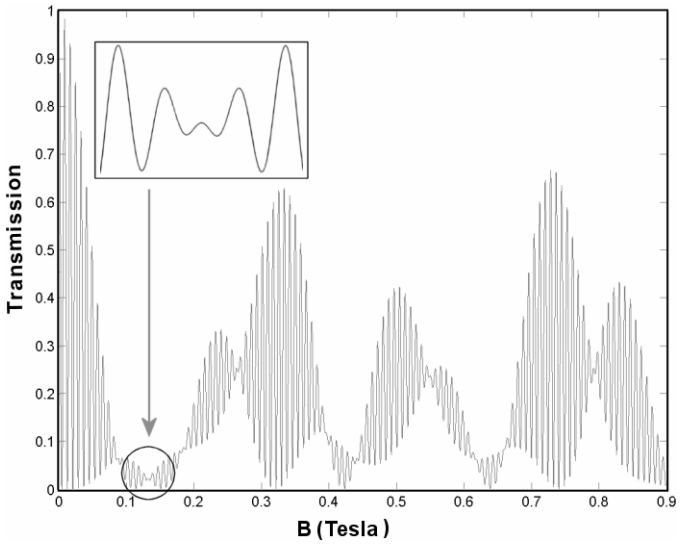


FIGURE 6.5: Magnetoconductance in units of $2e^2/h$ (Transmission), as a function of the applied field **B**. The inset shows details of the curve in the range 0.1-0.15 Tesla where beatings of the high frequencies components are visible.

Device geometry suggests that the data of group I are due to ring $\alpha$: higher frequencies correspond to quickly varying magnetic fluxes and, assuming the magnetic field does not lie too close to the xy plane, to wider ring's areas. The correctness of this assumption is strengthened by the fact that group I contains eight frequencies: this suggests again these data pertain to ring $\alpha$ (see Table 6.1). Consider now frequencies in group II: the fifth and the second frequency are respectively the sum and the difference of the fourth and first, hence 35.6560 Tesla$^{-1}$ and 17.1550 Tesla$^{-1}$ are very likely to be $|\omega_\beta|$ and $|\omega_\gamma|$ (see table reported in Table 6.1). By exclusion we have $|\omega_\delta| = 23.7707$ Tesla$^{-1}$. By inspecting the ratio between 23.7707 Tesla$^{-1}$ (third frequency in group II) and the candidates $|\omega_\beta|$ and $|\omega_\gamma|$ we can easily infer, from Eq.(6.6) and the rings areas, $|\omega_\beta| = 17.1550$ Tesla$^{-1}$ and $|\omega_\gamma| = 35.6560$ Tesla$^{-1}$ so that we finally have a coherent interpretation of frequencies of group II.

| | Frequencies (Tesla$^{-1}$) |
|---|---|
| group I | 733.6852 |
| | 750.8402 |
| | 757.4559 |
| | 769.3412 |
| | 774.6109 |
| | 786.4962 |
| | 793.1119 |
| | 810.2669 |
| group II | 17.1550 |
| | 18.5010 |
| | 23.7707 |
| | 35.6560 |
| | 52.8111 |

TABLE 6.2: Frequency spectra of the G(B) curve (see Fig. 6.5).

In conclusion, the possible directions of **B** are given by the unit vectors ($\pm$0.6124, $\pm$0.3536, $\pm$0.7071).

An important aspect, that concerns the possible range of device operation, it's worth being higlighted. As the measurement relies on quantum interference, the device is expected to work only as long as the electronic wavefunction is not significantly affected by the influence of the external magnetic field. In particular a very strong field can give problems at the branching points making it difficult to have a nearly equal transmission through the two arms of the rings. As an estimate, the device operation begins to be affected by the magnetic field when the magnetic lenght becomes smaller than the lateral dimensions of ring's quantum wires, i.e. 100 nm for the planar ring and 65 nm for the vertical ones. This estimate indicates 1 T as a limit field for the operation of the gradiometer.

## 6.4 Susceptibility measurement capability

Magnetism in nanoparticles has recently attracted a lot of interest in the scientific community. As particle's dimensions shrink, evidences of exotic and often unexpected magnetic phenomena arise. Shape anisotropy and wall energies come in to play, affecting magnetization as the volume to surface area ratio is reduced. Most of the devices so far proposed serve the scope of measuring magnetization intensity, that is a scalar quantity, while, to my knowledge, none of them allows to access direct information on the local magnetization anisotropy at the nanometer scale, further more in a non-invasive way. In the present section it is shown how the device proposed in this capter is suited to fill the gap as it could prove useful in determining the magnetic susceptibility tensor of nano-magnets.

The basic idea is to place a nano-particle in the etched hollow of ring $\alpha$ [3]. Application of an external field $\mathbf{H}$ induces a magnetic field $\mathbf{B}$ in the sample. As long as linear response holds, $\mathbf{B} = \mu\mathbf{H}$, $\mu$ being the magnetic susceptibility tensor. The device geometry is ideal for the scope, as ring $\alpha$ directly encapsulates the sample and the vertical rings lay in close proximity to the sample surface. By sweeping the external field in the $\mathbf{n}$ direction $\mathbf{H} = \mathbf{n}H$ and measuring the fundamental oscillation frequencies $\omega_i$, the device is actually selectively measuring some components of the magnetic susceptibility tensor, in fact

$$\omega_i = \frac{2\pi}{\Phi_0}\frac{d(\mathbf{S}_i \cdot \mu\mathbf{H})}{d(\mu_0 H)} = \frac{2\pi}{\Phi_0}\frac{\mathbf{S}_i \cdot \mu\mathbf{n}}{\mu_0}, \tag{6.8}$$

where again $\mathbf{S}_i = S_i\mathbf{n}_i$ with $\mathbf{n}_i$ indicating the surface unit vector of ring $i$ and $\mu_0$ being the magnetic permeability constant. Choosing as example $\mathbf{n} = \mathbf{z}$ the following are obtained

$$\begin{aligned}
\mu_{xz} &= \frac{\Phi_0}{2\pi}\mu_0 S_\gamma^{-1}\omega_\gamma, \\
\mu_{yz} &= \frac{\Phi_0}{2\pi}\mu_0 S_\beta^{-1}\omega_\beta, \\
\mu_{zz} &= \frac{\Phi_0}{2\pi}\mu_0 S_\alpha^{-1}\omega_\alpha.
\end{aligned}$$

[3] This can be done exploiting an atomic force microscope (AFM) or directly depositing a nanoparticle in ring $\alpha$ by standard evaporation or growth techniques; refer to the article T. Junno, K. Deppert, L. Montelius, and L. Samuelson, Appl. Phys. Lett. **66** 3627 (1995).

Directing the external field **H** along the **x** and **y** axis it is possible to measure the remaining terms of the tensor $\mu$. Note that the linear response hypothesis is not really necessary as the device works measuring the differential magnetic field **B**, so that the measurement will yield in general a $\mu(H)$. Nevertheless it is usually necessary to sweep the field on a significant range making it difficult to really determine the value of $\mu(H)$ at a specific **H**.

The device proposal here presented is easily integrable with other spectroscopic techniques; for example, to mention one, it could be integrated on the same Hall bar together with a micro-ballistic Hall magnetometer [57]. This would allow to obtain the sign of the diagonal tensor components $\mu_{ii}$, that is the diamagnetic or paramagnetic-like behavior of the nano-sized material.

## 6.5 Conclusions

In conclusion, a three dimensional interferometer relying on AB effect has been proposed. It has been shown how the device can operate as a nano-scale gradiometer. Its application in the study of nano-magnetism could allow to measure the absolute values of the magnetic susceptibility tensor components, locally, at the nanometer scale and non-invasively. The fabrication strategy has been outlined. A detaliled analysis of the heterostructure parameters has shown that the device proposal is well within reach of present day technology.

# Chapter 7

# Realization of Quantum Interference Devices

Two novel quantum interference devices are proposed and fabricated. These are vertical (interference plane laying perpendicular to the heterostructure layers) and planar (interference plane laying parallel to the heterostructure surface) interferometers. They exploit the coupled 2DEGs and the single 2DEG arising from the particular design of the $GaAs/AlGaAs$-based heterojunctions. The devices are realized with a lithographic pattern designed so as to serve on both structures. Design and characterization of the two heterostructures via cryogenic magneto-transport techniques, together with device pattern design, fabrication and preliminary characterization are reported.

## 7.1 Motivation

Ballistic transport in nanodevices is nowadays possible thanks to the growth of high mobility 2DEGS and to the availability of submicron processing techniques. It is also possible to exploit electron quantum coherence to control macroscopic quantities such as conduc-

tance. Further large-scale miniaturization is expected as a result of ever evolving processing technology. As gate dimensions become comparable to the electron coherence lengths, devices principles change drastically and the electronic transport can be dominated by coherence effects [10, 9]. Understanding and mastering the physics of quantum interference devices is the frontier of device and semiconductor physics. Quantum interference transistors (QUITs) require voltages orders of magnitude lower as compared to traditional FETs (millivolt as compared to Volt) [58]; this is very important to achieve lower power consumption and higher device integration. For these reasons several QUITs have been proposed and fabricated [59, 60, 61, 62, 63, 64].

The basic interference device is an Aharonov-Bohm ring, where two propagation paths are allowed to interfere. By controlling the phase difference between the two arms transconductance oscillations can be produced. This phase shift can be obtained in different ways, the most simple ones being the magnetic and electric AB effect. The former one is preferable as the observation of the magnetic AB effect usually requires large superconducting magnets and, in view of a possible device integration, a local control of the magnetic field. Another important issue with QUITs is the contrast of the conductance oscillations. High contrast is always desirable is view of practical applications, possibly in closed-cycle refrigerators.

## 7.2 Devices concept and proposal

### 7.2.1 *Vertical interferometer*

The vertical interferometer, fabricated as part of my thesis work, originates from a device realized by Piazza et *al.* [54]. The interferometer proposed in Ref. [54] performed extremely well as compared to previous devices reported in literature, showing an oscillation contrast $\sim 30\%$ when used in the electrostatic AB mode. The novel design here proposed (see Fig. 7.1) is expected to improve the device of Ref. [54]: the basic idea is to remove the series resistance due to the injector and collector of the previous device. In this way an higher contrast is expected, as oscillations originate just from a modulation of the resistance of the interference region.

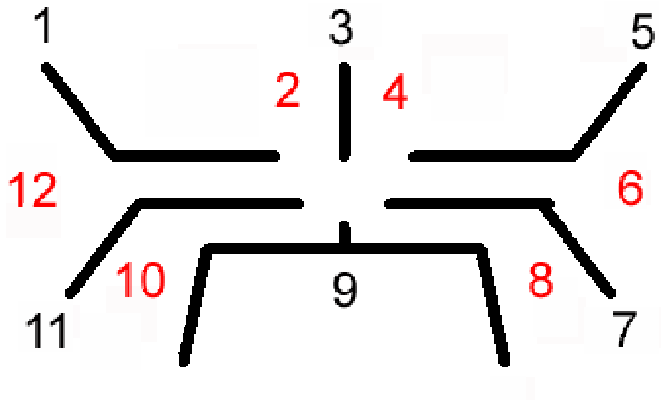


FIGURE 7.1: Scheme of the device. Red numbers label ohmic contacts. Black numbers label metal gates.

The novel design is composed of seven metallic gates and six ohmic contacts and is patterned on a $GaAs/AlGaAs$ heterojunction embedding a double 2DEG (the heterojunction similar to the one described in paragraph 6.3). New gates have been added (see Fig.7.1) with respect to the device pattern of Ref. [54] in order to achieve a better control of the quantum states involved in device operation. In addition, the device geometry has been modified in proximity of the interference region to allow a direct measurement of the conductance oscillations. This is expected to yield an higher oscillation contrast. Gates labeled 1, 5 and 9 are supposed to define the main transport channels and they should be biased down to complete depletion of the underlying electron gases. Polarization of these gates creates two 1D channel running in the center of the device, shown in figure 7.1, from left to right. This channel (for the moment gates 7 and 11 are not supposed to be biased) is analogous to the one illustrated in Fig. 6.4 (b), the only difference here is that the electron depletion is obtained by biasing the metal gates as opposed to etching of the heterostructure layers. The interfering paths of the device are positioned in the middle of the device where gates 7, 11, 9 and 3 converge and they are buried 70 nm beneath the surface. Gate 3 can be biased in order to apply an electrostatic field in the plane of the buried interferometer branches. By sweeping such field, one should produce conductance

oscillations due to the electric Ahoronov-Bohm effect. Gate 3 is positioned some hundreds nanometers sideway respect to the interference region, nevertheless it is easy to demonstrate that the polarization of such a gate will produce an electric field perpendicular to the electronic gases also in the central region. This field is provided by the *border effect* of gate 3. These field lines are expected to be oriented in a way similar to the the field lines present at the border of a finite parallel plates capacitor (in the device the plates are constituted by gate 3 and the 2DEG itself). The last two gates, labeled 7 and 11, are intended to control the subband population in the 1D channels formed by gates 1, 5 and 9. They should be biased so as to leave only one subband populated in the underlying heterojunction region (this situation is analogous to the one depicted in Fig. 6.4 (c)). It is important to note that these gates are not supposed to completely deplete the underlying 2DEG, but just to control the electronic density. As a consequence 2DEG regions labeled 6 and 8, as well as 10 and 12, will be actually shorted in the measurements. It is actually possible to insulate them by a proper biasing of gates 7 and 11, but this is not the proper procedure intended for device operation. In normal device operation ohmic contact 6 (and as a consequence 8) is grounded while ohmic contacts 10 (and 12) is connected to the excitation source. Ohmic contacts 2 and 4 are intended to serve as probes in a four-wire measurement. They should allow to measure the conductance directly at the boundary of the interference zone. Up to now the aim was to produce a phase shift between the propagation paths by biasing gate 3. A similar phase shift can also be induced by sweeping a magnetic field perpendicularly to the plane defined by the interfering paths. The mechanism is exactly the same as the one explained in paragraph 6.3 with regard to the vertical ring of the nano-gradiometer.

### 7.2.2 *Planar interferometer*

The gating pattern presented in the previous section can also be exploited to define a *planar* interferometer when patterned on a single 2DEG heterostructure. The working principle is as follow. Gates 1, 3, 5, 7, 9 and 11 have to be biased so as to pinch off channels 2 and 4 and to completely deplete the 2DEG underlying each gate. In so doing four waveguides, connected to ohmic contacts 6, 8, 10 and 12, are obtained. Contacts 10 and 12, as well

as 6 and 8 will now be independent, differently from the *vertical* interferometer case. The basic idea now is to inject carriers into one of the waveguides, for instance from contact 12, and to measure how the current branches between waveguides ending on contacts 6 and 8. To this end contact 10 is left floating, whereas contacts 8 and 6 are grounded. An excitation voltage is applied in between contact 12 and ground. The situation is depicted in Fig. 7.2: the gates have to be biased in order to

- achieve a single populated propagating channel (of transverse energy $E_{x1}$) in the emitter and collectors waveguides;
- achieve two populated 1D subbands (with transverse energy $\tilde{E}_{x1}$ and $\tilde{E}_{x2}$) in the interference region (see Fig. 7.2).

Electrons propagating through the device will enter the interference region from the emitter and oscillate, once in the interference region, along the x direction with a frequency $\tilde{\omega} = (\tilde{E}_{x2} - \tilde{E}_{x1})/2\hbar$. As a result, modulating $\tilde{\omega}$ and/or the interference region length will modulate transmission probabilities to the collector *c1* or *c2*. This transmission modulation can be controlled by appropriate gate biasing so that the device constitutes a transistor. Modulation of frequency $\tilde{\omega}$ can be achieved by changing the lateral width of the interference region, which in turn is related to the difference $\tilde{E}_{x2} - \tilde{E}_{x1}$. This lateral width can be controlled by sweeping the bias applied to gate 3. In addition, the length of the interference region can be controlled sweeping the bias applied to gate 7 and/or 11 (this also affects the emitter and collector lateral width, hence the mode in the emitter and collectors region).

## 7.3 Heterostructure design and characterization

In this section a description of the heterostructures, used to fabricate the above-mentioned devices, is presented. Different heterostructure designs were numerically investigated in order to tailor the desired band structure. The simulations were performed solving self-consistently the Poisson-Schrödinger problem at 4.2 K. The numerical code was implemented by Vincenzo Piazza [65]. The two final heterostructures were grown by MBE at Cavendish Labs in Cambridge, UK. SdH and Hall measurements were performed to check

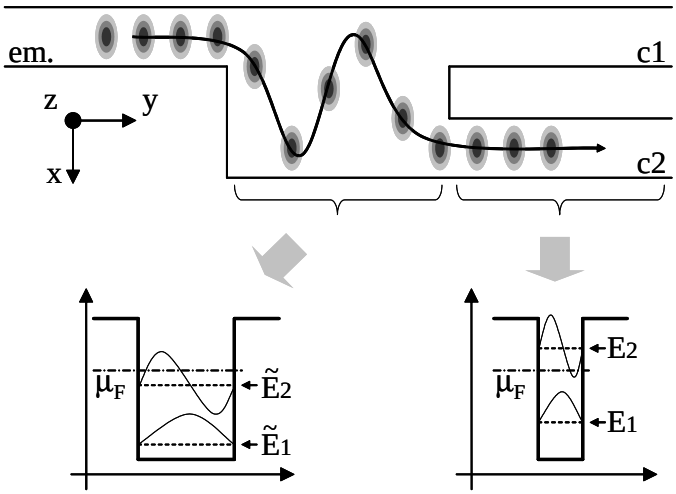


FIGURE 7.2: Device scheme resulting from the bias situation described in the text. This configuration gives rise to the planar interferometer. The gray spots reppresent the electron probability density propagation. The two collectors are denoted by *c1* and *c2*. The emitter is denoted by *em*. The interference zone is where lateral (with respect to propagation direction) oscillations of the electron probability density take place. Quantum wire lateral potential and eigenvalues in the emitter and collector region (bottom-left scheme) and in the interference region (bottom-right scheme) are shown. The quantum wire lateral potential is approximated with an infinite rectangular quantum well. $\widetilde{E}_{x1}$ and $\widetilde{E}_{x2}$ are the first two transverse eigenvalues, $\mu_F$ is the chemical potential.

if the structures matches the desired parameters in terms of carrier density and number of occupied subbands after gate deposition. The dependence of this parameters vs. an applied gate voltage was also explored.

### 7.3.1 *Description of the experimental set-up*

The measurements here reported were performed in a Heliox $^3He/^4He$ cryostat at temperatures down to 300 mK. Magnetic fields were generated by a superconducting-NbTi-solenoid magnet immersed in a liquid-He bath. Hall bars were fabricated via optical lithography and

etching techniques. AuGe/Ni/Au ohmic contacts were then fabricated and a Au Schottky gate evaporated on the sample surface to control the charge density in the 2DEG. Refer to the Appendix A for further technical details. Resistances $R_{xx}$ and $R_{xy}$ *vs.* gate bias were measured in the SdH and Hall regimes in a four-wire Hall configuration. The excitation-current level $I$ was set such that the voltage drop across the device was always less than $k_BT/e \sim 30\mu$V at $T$= 300 mk, [1] as required to avoid electron heating effects. The current was modulated at a frequency of 17.3 Hz and the voltage signal was measured with a standard lock-in technique. The DC bias was provided to the Schottky gate by means of a 16-bit digital-to-analog converter (DAC) DAC488HR/4. The DAC output was filtered with passive RC filters (time constant $\sim$ 0.3 s) to protect the device from voltage spikes. A $n^+ - GaAs$ LED, placed on the cryostat sample holder, allowed to illuminate the sample at low temperature so as to induce persistent photoconductivity in the 2DEG. In the following the two heterostructures will be characterized: $A2092$ (double 2DEG for the vertical interferometer) and $A2088$ (single 2DEG for the planar interferometer).

### 7.3.2 *Double two-dimensional electron gas: A2092*

The clue element to achieve the vertical interferometer geometry is an $GaAs/AlGaAs$ quantum well, where two coupled subbands arise as a consequence of the electrostatic barrier present on the bottom of the quantum well. The heterostructure is similar to the one discussed in chapter 6. The composition of the heterostructure, named A2092, is reported in Table 7.1.

The number of occupied subbands, after illumination, was determined by SdH measurements, as outlined in section 2.2.2. The excitation current was set to 85 nA. The same notation as in section 2.2.2 will be used if not otherwise stated. The voltage $V_{xx}$ is measured vs. the field intensity $B$ for different gate biases [2]. Figure 7.3 reports a schematic picture of the experimental setup. The resistance $R_{xx}$ is then plotted vs. $1/B$ and the Fourier transform is taken. The resistance $R_{xx}$ vs. $1/B$, at a gate bias $V_g$=0, is reported in Fig. 7.4. The frequencies $B_j$, at which peaks of the Fourier transform spectrum occur, are related to the sheet electron density $n_j$ in each subband $j$ by the

[1] $k_B$ is the Boltzmann constant

[2] the magnetic field is perpendicular to the 2DEG

| Material | Thickness (nm) |
|---|---|
| GaAs | 10 |
| $Al_{0.33}Ga_{0.67}As : Si$ | 40 |
| $Al_{0.33}Ga_{0.67}As$ | 20 |
| GaAs | 60 |
| $Al_{0.33}Ga_{0.67}As$ | 2.5 |
| GaAs | 11 |
| $Al_{0.33}Ga_{0.67}As$ | 22.5 |
| $Al_{0.33}Ga_{0.67}As : Si$ | 40 |
| AlGaAs-GaAs substrate | 1300 |

TABLE 7.1: Heterostructure A2092 layers. The $Si$ doping concentration is $2 \times 10^{18} cm^{-3}$.

relation: $n_j = 2eB_j/h$. Figure 7.5 reports the electron densities in the two subbands as a function of $V_g$. Data from the Fourier transform spectrum, at $V_g$=0, indicate a sheet electron density of $n_1 = 5.5 \times 10^{15}$ m$^{-2}$ and $n_2 = 3.2 \times 10^{15}$ m$^{-2}$ for the first and second subband respectively. Figure 7.5 demonstrates that for $V_{gate} \leq$-0.7 Volt only one subband is occupied, whereas for $V_{gate} \geq$-0.7 Volt two subbands are occupied, thus proving that the designed heterostructure allows to tune the number of occupied subbands.

Hall measurements were also performed. The experiment was carried out with the same excitation source as before, the difference with the SdH measurement being twofold: the voltage $V_{xy}$ is measured and the applied magnetic fields are lower. See Figure 7.6 for the experimental set-up. For the Hall bar in use $L$=120 $\mu$m and $W$=80 $\mu$m. The electron sheet density $n_e = BI/eV_{xy}$ resulting from Hall measurements is, at zero gate bias, $9.0 \times 10^{15}$ m$^{-2}$. The electron mobility, obtained as described in section 2.2.2, is $\mu = 1.48 \times 10^2$ m$^2$/V·s. Such an high mobility value indicates a low scattering probability for electrons, hence suggesting longer coherence lengths.

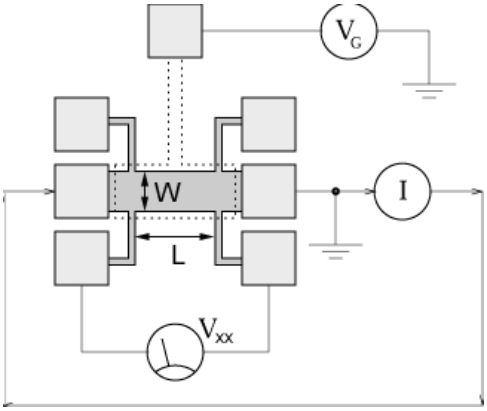


FIGURE 7.3: Schematic representation of a SdH measurement setup. The dotted line encloses the area on which the metal gate is deposited. The magnetic field is perpendicular to the figure plane.

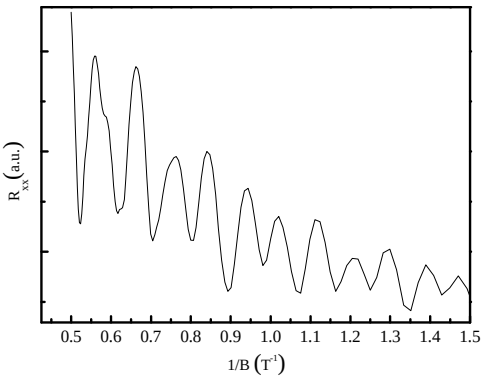


FIGURE 7.4: The longitudinal resistance $R_{xx}$ vs $1/B$ at a gate bias $V_g$=0.

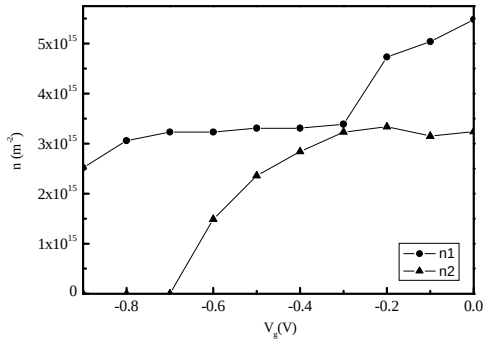


FIGURE 7.5: Electron densities in the two subbands of A2092 as a function of $V_g$. Dots are inherent to the electron density in the subband with lower energy, whereas triangles indicate the electron density of the higher energy subband. Starting from positive $V_g$ the low-energy subband is the first to be affected by the external field, as its electronic distribution is positioned *closer* to the gate. At $V_g$=-0.3 Volt there is a cross-over between the two subbands: this corresponds to swap of spatial position between the electron distribution of the two subbands. For further negative biases the higher energy subband electron distribution, which now resides closer to the surface, starts to be depleted while the low-energy subband is now shielded from the electric field. Finally when the higher-energy subband is completely depleted, depletion of the low-energy subband continues [53] down to pinch-off.

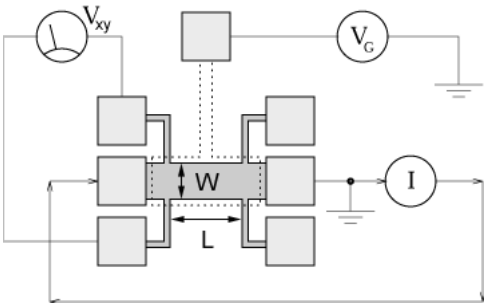


FIGURE 7.6: Schematic representation of a Hall measurement setup. The dotted line encloses the area on which the metal gate is deposited. The magnetic field is perpendicular to the figure plane.

### 7.3.3 *Single two-dimensional electron gas: A2088*

The composition of the heterostructure A2088 is reported in Table 7.2. The same char-

| Material | Thickness (nm) |
|---|---|
| GaAs | 10 |
| $Al_{0.33}Ga_{0.67}As : Si$ | 40 |
| $Al_{0.33}Ga_{0.67}As$ | 20 |
| GaAs | 167 |
| AlGaAs/GaAs substrate | 1000 |

acterizations as for A2092 were performed on the present sample. Only one subband was found populated with no gate bias, thus confirming A2088 as a single 2DEG structure. The relevant figures for the heterostructure in question are a sheet electron density $n_e = 3.0 \times 10^{15}$ m$^{-2}$ and an electron mobility $\mu = 1.1 \times 10^2$ m$^{-2}$/V·s at 300 mK, after illumination.

## 7.4 Devices realization

In this paragraph device patterning techniques and fabrication strategy are outlined, together with preliminary measurement performed to verify the fulfillment of the basic device characteristics:

- the transition from 2DEG to a one-dimensional channel by biasing gates 9, 1 and 5 (see Fig. 7.1);
- tuning of structure *A*2092 as a single and double 2DEG as a function of the top gate bias.

### 7.4.1 Device fabrication

Patterning of the device has been performed with a LEO 1525 SEM, based on a Gemini thermal field emission column, modified for EBL. The electrostatic beam-blanker was made by Raith. The exposition is fully controlled by a Nabity System pattern generator software. The control software comprises a CAD program allowing to design the lithographic pattern with full control on the exposure parameters. Tackling the desired design is a time consuming process. Many trials are needed to find the optimal design and exposure parameters. The ultimate CAD lithographic project is illustrated in Fig. 7.7 and comprises three layers (one color per layer). Each layer can be thought as an independent exposure session, in that the main exposure parameters are changed from one layer exposure to the next one. The smaller features are comprised in the yellow layer, whereas the coarse structures are part of the purple layer. The purple layer contains the patterns that connect the interferometer Schottky gates with the metal gates patterned by optical lithography. The latter terminate in gold pads ($200\mu$m$\times 200\mu$m) accessible for bonding, thus allowing to contact the device on a dual in line (DIL) support and to measure it. The definitions and concepts used in EBL will not be reported here and can be found in [8, 66, 67, 68, 69]. The fine features (yellow layer) were exposed setting an area dose 280 $\mu$C/cm$^2$, a dwell time of 20.4 $\mu$sec and a measured beam current of 20 pA. The coarse features (purple layer) were exposed setting an area dose D= $300\mu$C/cm$^2$, a dwell time of 14.3 $\mu$sec and a measured beam current of 339 pA. The blue layer was used to expose vertical lines that are intended to improve mechanical resistance ad adhesion of gates 7 and 11 of the interferometer. A line dose 2.7 nC/cm, a dwell time of 162.9$\mu$sec and a measured beam current of 20 pA where used. Detailed view the yellow layer is reported in Fig. 7.8. All the exposures were performed using an acceleration voltage of 30 kV. The writefield size dimension for the fine feature layer was obviously smaller than the writefield size dimension for the coarse feature layers.

Before e-beam exposure, a thin layer ($\approx$ 200 nm) of positive e-beam resist (950 K PMMA) is deposited and spun on the sample surface. The sample, at this stage, has already undergone extensive processing and h already been divided into electrically isolated islands known as mesas. Each island is a suitable 'work bench' providing ohmic contacts to the 2DEG and conducting pads for electrical connections with a dual-in-line (and,

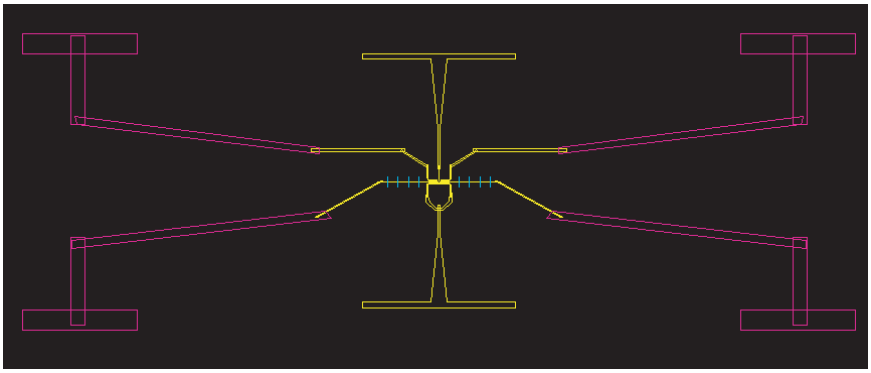

FIGURE 7.7: The CAD project for the realization of the device. The three colors indicate different project layers. The write field sizes change from layer to layer. The exposure parameters such as doses, scan mode, dwell time change from feature to feature. The purple layer serves the scope of contacting the interferometer gates (yellow layer) with the gates patterned via optical lithography.

ultimately, to lab instruments). The nanogates are fabricated on one of these mesas. After exposure the resist is developed. The molecular chains, broken by the electronic beam, become more soluble than the unexposed ones, as a result the developer only removes the exposed resist. After development, Cr/Au metal gates are deposited with a thermal evaporator in vacuum (pressure $\sim 10^{-7}$ Torr). After evaporation the sample is left in warm acetone for some time (ranging from 10 minutes to several hours). Acetone removes the resist so that only the metal deposited directly on the sample surface remains, reproducing the shapes of the exposed pattern. Details of all the processing steps followed in this work are reported in Appendix A. SEM images of the details of the interferometer, together with its dimensions, are shown in Fig.7.9. More SEM images of the interferometer, taken at lower magnifications, are shown in Fig.7.10. The pictures show how the lithographic project, together with optimal control of the processing steps, led to a very fine device.

The next step is to provide a way to contact the Schottky gates of the interferometer to lab instrumentation. This is done by patterning big metallic pads and connections via optical lithography. A mask with the desired pattern was designed using a CAD. This

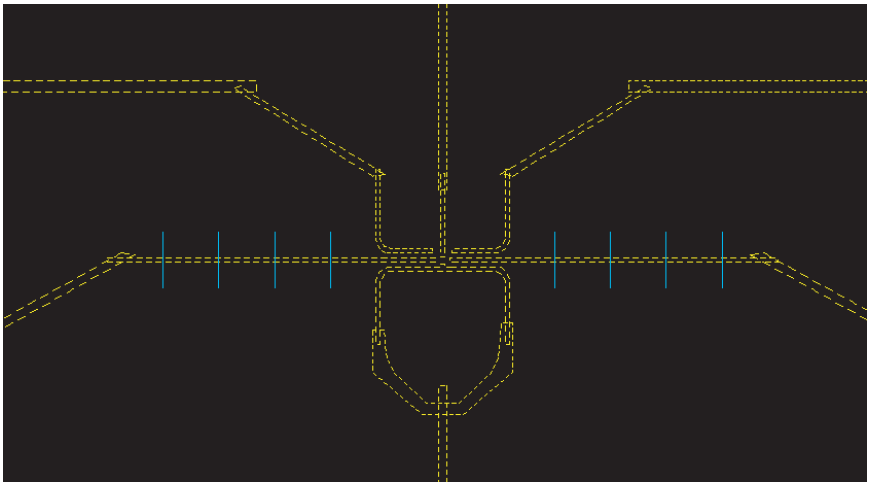

FIGURE 7.8: Detail of the project. In the present figure the interferometric part of the device is reported. The vertical bars have been added to guarantee mechanical stability of the two central fingers.

lithographic process is very similar to the one used for nano-gate fabrication, the main difference being the substitution of e-beam resist with positive photoresist (S1818) and use of UV light instead of electrons. The mask aligner used for optical lithography was a Karl Suss MJB3, equipped with a UV lamp emitting light at a wavelength of 365 nm . Details of the processing steps are given in Appendix A. The result is reported, in order of decreasing magnification, in images taken at the optical microscope, see Fig. 7.11 and Fig. 7.12. Only the device fabricated on the substrate A2092 is reported in the figures, the fabrication strategy and outcome for the device fabricated on substrate A2088 being the same.

### 7.4.2 Preliminary characterization

Preliminary devices characterization measurements are reported. These measurement were intended to check if the devices were potentially suitable to work as interferometers. Only

the measurements for the vertical interferometer are reported, characterization of the planar interferometer being very similar and giving positive results.

All gates were electrically tested for leakages in the temperature range comprised between 4.2 K and 300 mK. Vanishing leakage currents (resistance $\gg 10$ G$\Omega$) were detected within the applied voltages range (0 to $-4$ V), proving the good quality of the processing involved in gates deposition.

The first measurement presented is intended to check if, by appropriately biasing the gates couples $1-9$ and $5-9$, the current flow can be constrained to the ideal channel pattern reported in Fig. 7.13. As a function of the gate bias a transition from a 2DEG to a 1DEG (quantum confinement in two directions) is observed as a sharp step in the conductance (see figure 7.14). Two-probe measurements were performed at 4.2 K, with an excitation voltage of $\approx 30\mu$ V at a frequency of 17.3 Hz between contacts 12 and 6. For gate biases down to -0.8 V the 2DEG beneath the gate is still conducting while at -0.8 V it is completely depleted, this results in a sudden drop in conductance. Further lowering the bias the channel lateral dimension is reduced hence leading to a further and continuous decrease of the conductance. Channel pinch-off can not be reached within the reported biasing range (in order to avoid device damage, no further increase in bias modulus was attempted). Refer to Fig.7.14 for the experimental data. This problem is not a severe one as gates 1, 5 and 9 are only intended to *define* the conducting channels. A complete pinch off can still be achieved biasing the control gates 7 and 11 (for instance the constrictions can be pinched off with gates 1, 5 and 9 at $-2.75$ V, and gates 7 and 11 at $-0.75$ V).

In order to test the tunability of the interference region, conductance was measured sweeping biases applied to gates 3 and 9. Complete pinch-off and conductance steps were observed, as predicted for a standard quantum point contact. Moreover *double* steps were also observed (see Fig.7.16): these *anomalous* steps indicate the presence of a double 2DEG constriction [53]. It is thus demonstrated that it is possible to have two geometrically separated interference paths in the central region. As a consequence, in principle, both electric and magnetic AB effects can be exploited. Refer to Figures 7.15 and 7.16 for the experimental set-up and the measured data.

The aim of this part of my thesis work was to explore the feasibility of devices operation. Work is in progress to find the ideal biasing situation and eventual modification to the

design for the devices to actually work as interferometers.

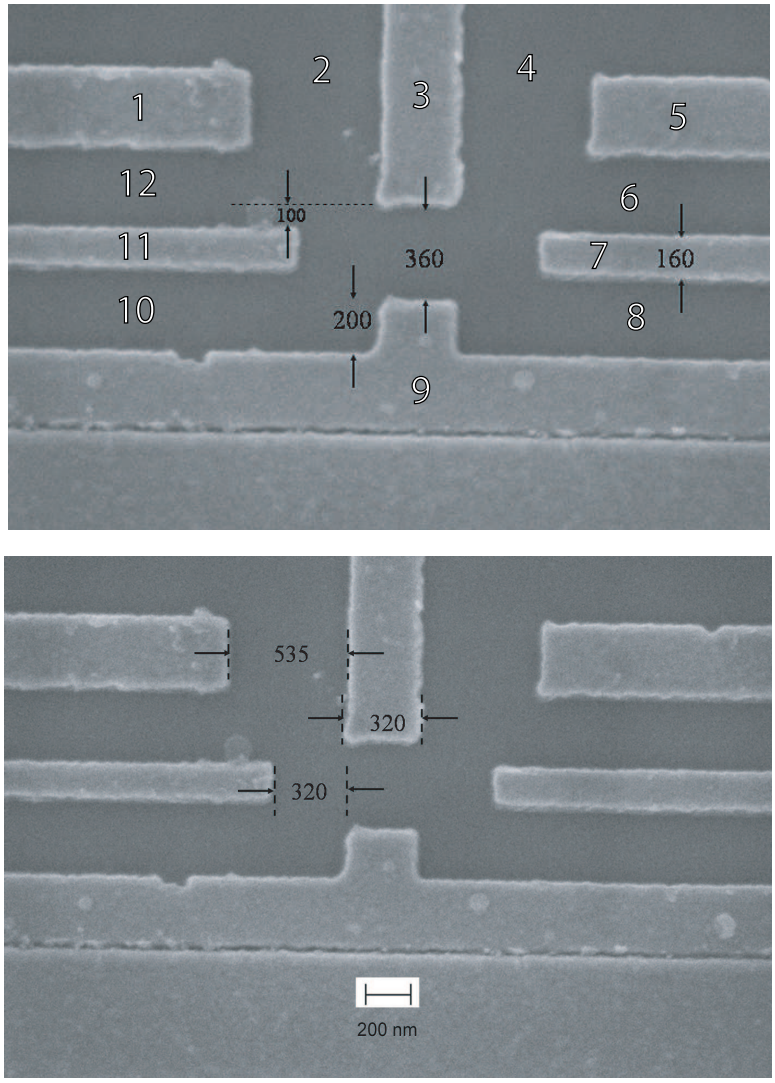


FIGURE 7.9: SEM image of the interference zone. Sizes are given in nm. The big numbers label the ohmic contacts and the metal gates according to the definitions of Fig.7.1.

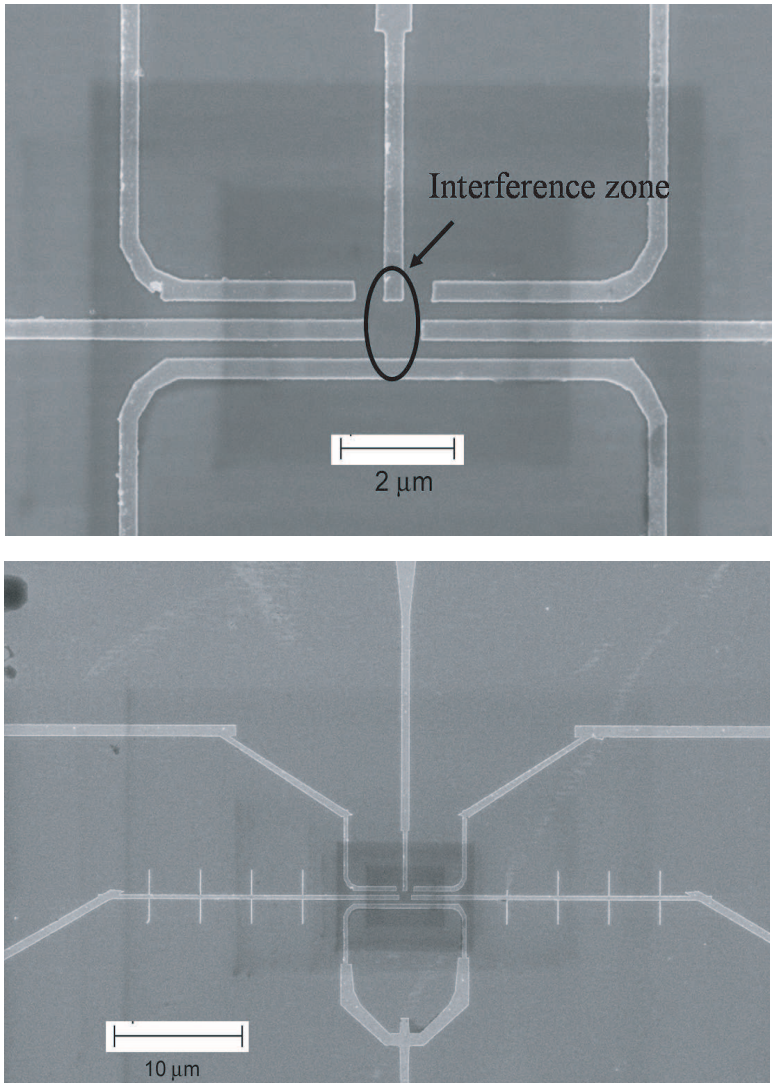


FIGURE 7.10: SEM image of the interferometer at two different magnifications. The interference zone, shown in details in Fig. 7.9, is indicated.

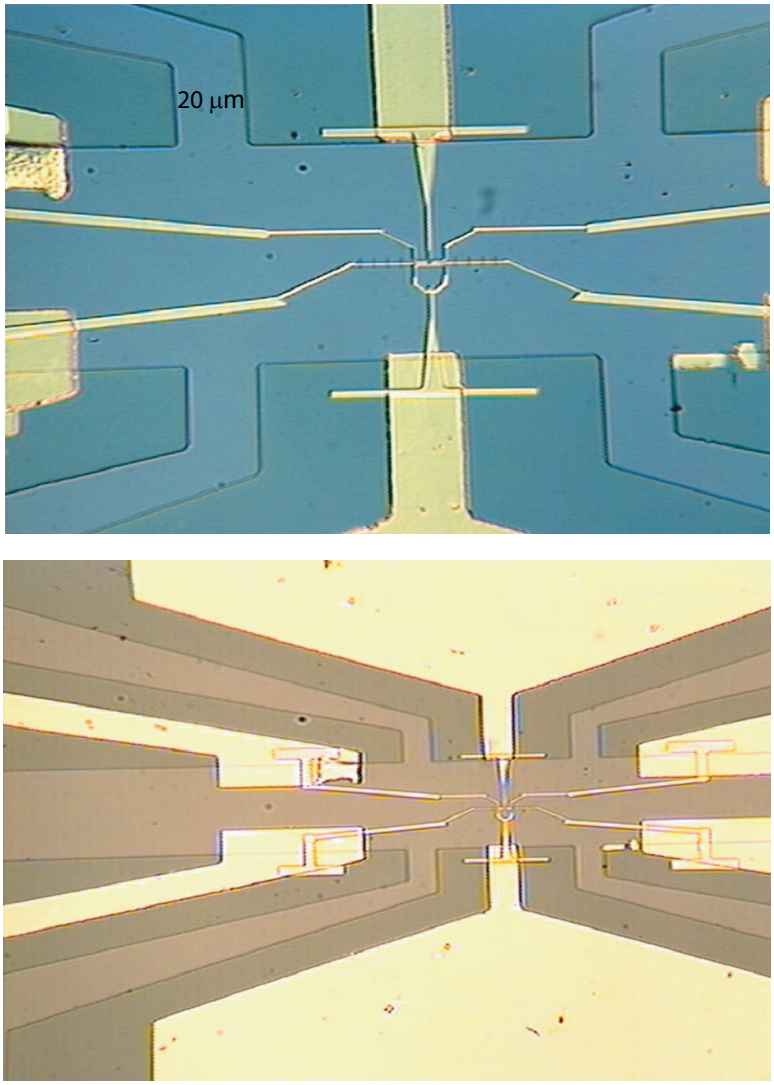


FIGURE 7.11: Images of the device and particular of the Hall bar taken with an optical microscope. Big metal gates patterned by optical lithography are clearly visible. These gates have been exposed and evaporated on top of the fine gates patterned by EBL.

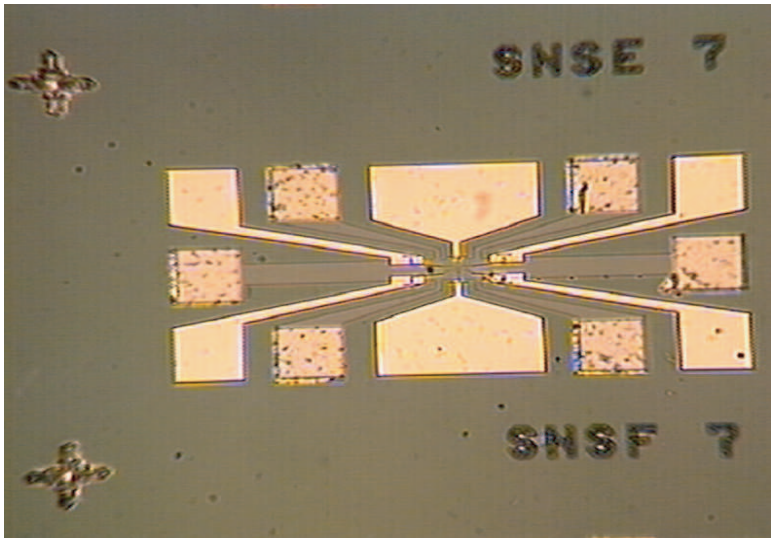


FIGURE 7.12: Image of the device and Hall bar taken with an optical microscope. Contacts pads are clearly visible, together with the etched mesa. The contact pads are squares with edges of 200 $\mu$m. The ohmic contacts pads are dark yellow, where is the Au gates are the bright yellow features.

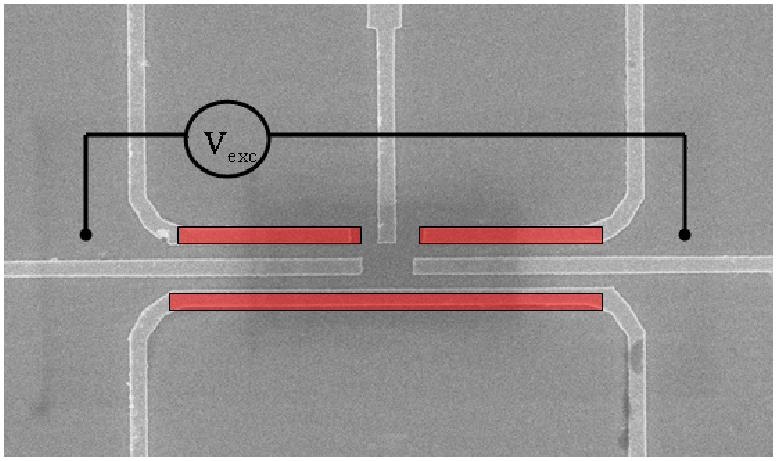


FIGURE 7.13: Experimental set-up to measure transition from a 2DEG to a 1DEG configuration. A bias voltage $V_b$ is applied to the red gates. $V_{exc}$ is the excitation voltage.

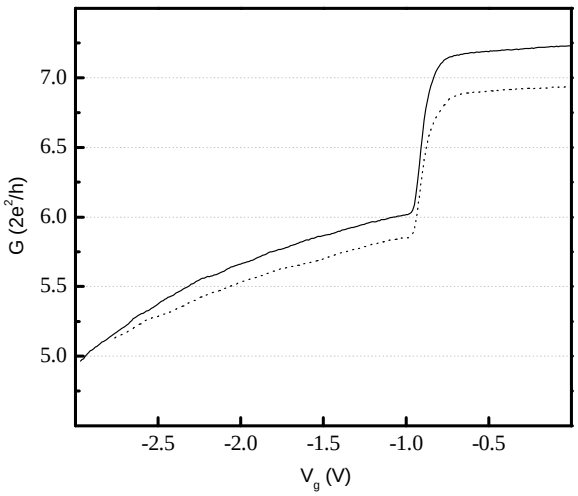


FIGURE 7.14: Conductance vs gate bias $V_g$ applied to gates 1-9 (continuous line) and 5-9 (dotted line) respectively. This measure has been obtained at a temperature of 4.2 K.

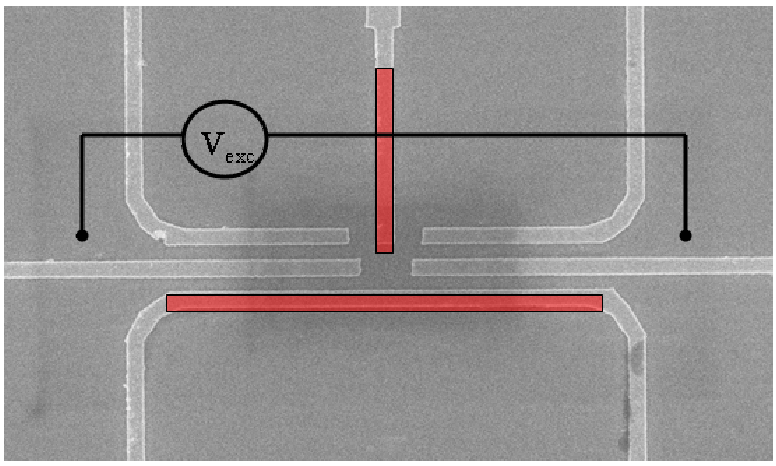


FIGURE 7.15: Experimental set-up to measure subband tuning capability in the interferometer region. A bias voltage $V_b$ is applied to the red gates. $V_{exc}$ is the excitation voltage.

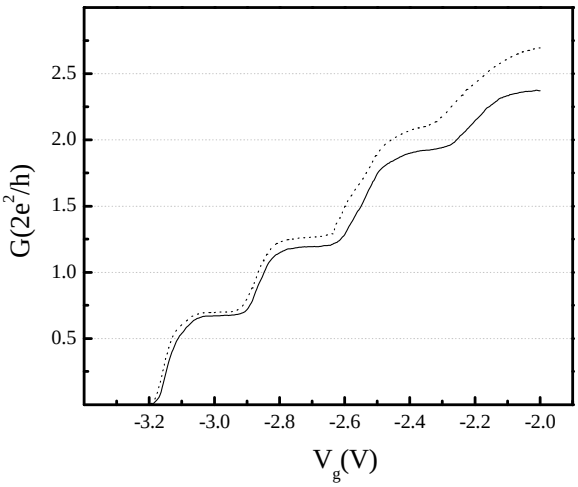


FIGURE 7.16: Conductance vs gate bias $V_g$ applied to gates 3-9. The solid and dotted lines refer to measurements performed at 4.2 K and 300 mK respectively. Conductance quantization steps are clearly visible. The first two steps have a step height of $0.7 \times 2e^2/h$, whereas the third step has a step height of $1.4 \times 2e^2/h$, for this reason it is named *double* step. *Double* steps indicate the presence of a double 2DEG constriction [53].

## 7.5 Conclusions

Two novel quantum interference devices have been proposed and fabricated. The devices exploit the coupled 2DEGs and the single 2DEG arising from the particular design of the $GaAs/AlGaAs$-based heterojunctions. The heterostructures have been characterized by cryogenic magneto-transport techniques. Material processing and lithographic techniques have been optimized resulting in two devices with very fine features. Preliminary characterization of the fabricated devices gave good results, indicating that the work done is proceeding on the correct track.

# Chapter 8

# Conclusions

In this thesis work aspects of electron dynamics in low dimensional systems based on metal surfaces and semiconductor heterojunctions have been investigated. The investigated systems are based on two dimensional electron gases.

The first part of this thesis work dealt with electron dynamics in surface-based 2DEGs, studied via multi-photon photoemission spectroscopy. The intrinsic linewidths of the electrons in the n=1 IPS on Ag(100) have been measured at different values of the parallel momentum. The spread in $k_{\|}$, due to the geometrical acceptance angle of the ToF, have been taken into account. It has been shown that, at $k_{\|}$=0, the contribution to the linewidth due to quasi-elastic scattering can be neglected. The experiments evidenced a much more rapid intrinsic linewidth broadening versus $E_{\|}$ on Ag(100) with respect to Cu(100), indicating that further theoretical investigation is needed to assess the IPS decay mechanism in Ag(100). Experimental evidence of multiphoton electron photoemission from the Ag(100), detected either with *p*- and *s*-polarized light, has been shown. The latter is a transition forbidden by the polarization selection rules. The violation of these rules is consistent with an interaction between the hot electron gas, generated in the non-linear absorption process, and the electrons in the IPS. Further on, for the first time, unambiguous evidence of an above threshold photoemitted Fermi edge in solids has been shown.

The second part, more technical in nature, concerned the design and development of new quantum interference devices. Design and characterization of the heterostructures were presented, together with devices construction schemes. Preliminary measurements were also reported, indicating the work has been moving on the correct track. A theoretical proposal for a three-dimensional quantum interference device, potentially serving as a nano-gradiometer, was also shown and numerically investigated. Its application in the study of nano-magnetism could allow to measure the absolute values of the magnetic susceptibility tensor components, locally, at the nanometer scale and non-invasively. The fabrication strategy has been outlined. A detaliled analysis of the heterostructure parameters has shown that the device proposal is well within reach of present day technology.

# Appendix A

# Influence of the spectrometer resolution on intrinsic linewidth measurements at $\mathbf{k}_{||} \neq 0$

Relaxation processes of IPS are very important for the study of surface phenomena, such as electronically induced adsorbate reactions or electron transfer across interfaces [9-10]. Electrons excited in IPS states are subject to decay due to scattering with electrons in the underlying bulk states. These scattering processes, due to the overlapping between the image state wave function and bulk states [11], can be classified in interband and intraband processes. The final state of the intraband process is an IPS state whereas the final state of the interband decay channel is a bulk state [12]. As a general rule, a broadening of the intrinsic linewidth with respect to normal emission (k//=0) is observed when a IPS is measured at a parallel momentum different from zero. The k//-dependence of the

broadening is different for interband and intraband processes. In this frame knowledge of the intrinsic linewidth as a function of parallel momentum helps discriminating which mechanism contribute to the IPS decay. Since IPS are a promising model system for a detailed understanding of fundamental mechanism of electron dynamics at surfaces, such measurements may contribute to the development of refined theoretical models. To achieve a better estimate of the intrinsic linewidth we propose a new fitting procedure that accounts for the influence of the angular acceptance of the detector. The prediction of this improved fitting procedure are tested comparing measurements taken with two Tof that have different angular resolution.

## A.1 Problems $\mathbf{k}_{||}$*resolution* : *anewFittingprocedure*

In Fig. 3.1 the 2PPE spectra at a photon energy of 4.32 eV and at $k_{\|}$=0 with the high resolution ToF (a) and with the low resolution ToF (b), respectively, are shown.

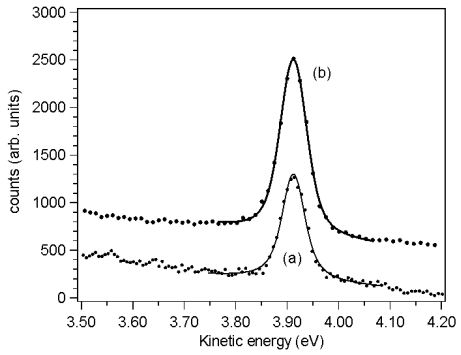


FIGURE A.1: Two-photon-photoemission spectra at a photon energy of 4.32 eV and at $k_{\|}$=0 collected with the high resolution (a) and the low resolution ToF (b). The feature at about 3.9 eV kinetic energy is ascribed to the n=1 image potential state. The lines represent the fit of the n=1 IPS with a lorentzian convoluted with a gaussian.

The effective mass associated with the n=1 IPS electrons have been measured in a previous work along the direction of the surface Brillouin zone (SBZ), resulting in a value

of 0.97±0.02 in free-electron mass units [17]. The binding energy [1] of n=1 IPS feature is 0.4±0.1eV in agreement with the values reported in the literature [3]. The two sets of photoemission measurements are collected by changing the angle between the normal to the sample and the ToF axis, along the $\overline{\Gamma X}$ symmetry direction of the Ag(100) SBZ in order to trace the $k_{\|}$-dispersion of the IPS states [17]. In order to estimate the intrinsic linewidth, a study of the lineshape of these states is presented. In particular, the n=1 IPS feature is fitted with a lorentzian convoluted with a gaussian. The linewidth of the lorentzian is considered as a parameter in the fit, whereas the gaussian linewidth ($\sigma$), which accounts for instrumental resolution, has been estimated for both ToF spectrometers and kept fixed. The gaussian linewidth depends on the spectrometer resolution and the laser linewidth. The laser linewidth is the same for the two set of measurements: about 12 meV. The spectrometer resolution depends on the geometrical area of the multichannel plate and on the electronics temporal resolution. The estimated linewidth of the gaussian is about 45meV for the low resolution ToF and 35meV for the high resolution spectrometer. These values are confirmed by fitting the Fermi-edge measured with single photon photoemission at a photon energy of 6.28 eV on Ag(100) cooled at 160K. An isotropic emission of the photoelectrons is considered in the following. Once the gaussian linewidth is fixed, the intrinsic lorentzian linewidth is estimated by the fit.

In Fig. 3.2, the behavior of the intrinsic linewidths against the parallel energy is showed for the two sets of experiments (a,c). The parallel energy is calculated using the following relations:

$$E_{\|} = \frac{\hbar^2 k_{\|}^2}{2m^*} \tag{A.1}$$

$$k_{\|} = \frac{\sqrt{2m^* E_{kin}}}{\hbar} \sin\theta \tag{A.2}$$

where $E_{kin}$ is the photoelectron kinetic energy and $\theta$ is the angle between the perpendicular to the sample and the ToF. The intrinsic linewidth measured at $k_{\|}$=0 with the high resolution ToF (15±2 meV) is in agreement with that obtained with the low resolution ToF (14±2 meV). The inverse linewidth (47±7 fs), is in agrement with time-resolved measurements on Ag(100) previously reported in literature [19]. At $k_{\|}$=0.14 $\mathring{A}^{-1}$, which

[1] the binding energy is measured with respect to the vacuum level

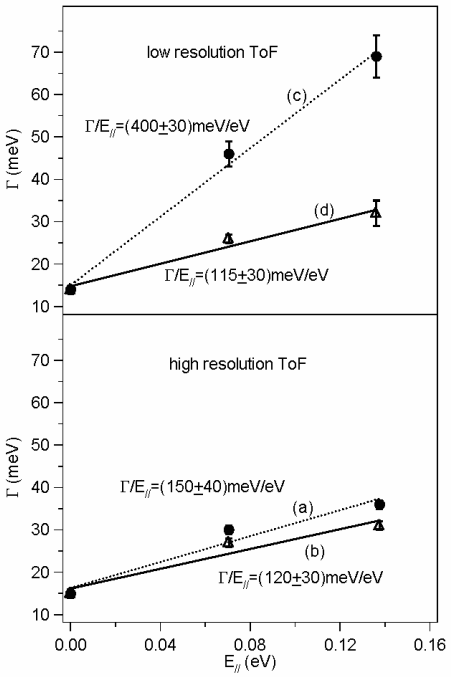


FIGURE A.2: The behavior of the intrinsic linewidth against the parallel energy is shown for the high and the low resolution ToF by fitting the IPS lineshape with a lorentzian convoluted with a gaussian ((a) and (c)) and with an integral of lorentzians convoluted with a gaussian ((b) and (d)). The lines represent the best linear fit of the experimental data (markers). The slopes are reported in the figure.

corresponds to an angle of 8°, the intrinsic linewidth measured with the high resolution ToF is about 20 meV smaller than the value measured with the low resolution ToF. The slope of the best linear fit of $E_{\|}$-dependent intrinsic linewidth obtained with the low resolution ToF is 400±0 meV/eV, whereas the slope with the high resolution ToF is about 150±40 meV/eV (Fig. 3.2). The difference of linewidths of the two measurements (using high and low resolution ToF) can be ascribed to a spread in $k_{\|}$. The geometrical acceptance angle of the ToF implies that, at a specified angle, the ToF simultaneously collects

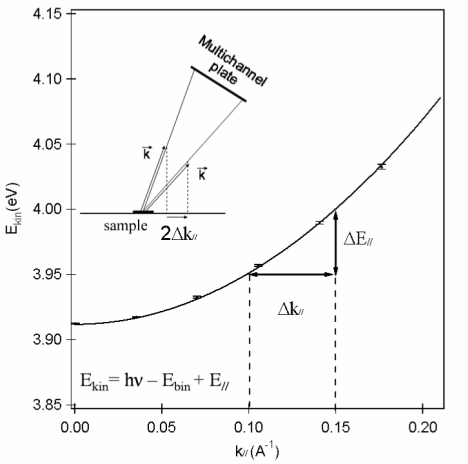


FIGURE A.3: In this figure the $k_{\|}$-spread related to the geometrical acceptance angle of the low resolution ToF detector is shown. At a specified angle, the detector collects photoelectrons with a different $k_{\|}$, therefore a sum of lorentzians each for a different $k_{\|}$ in the $k_{\|}$ range has to be considered in the fitting procedure. Due to the parabolic behavior of the kinetic energy versus $k_{\|}$, the $E_{\|}$-spread related to the $\Delta k_{\|}$ increases with $k_{\|}$. In the figure the experimental data (markers) are fitted with a parabolic curve (solid line), as discussed in Ref. [17].

photoelectrons with different $k_{\|}$-vector, see Fig. 3.3.

In particular, for the low resolution ToF the maximum $\Delta k_{\|}$ spread is about 0.045 $\mathring{A}^{-1}$, whereas for the high resolution ToF $\Delta k_{\|}$ is about 0.015 $\mathring{A}^{-1}$. Therefore, each spectrum is expressed as a sum of lorentzians with different $k_{\|}$. Due to the parabolic $k_{\|}$ dispersion, each of these lorentzian correspond to a different kinetic energy value. To reconcile the intrinsic linewidth values measured with the two spectrometers, the IPS feature has to be fitted with a convolution of a gaussian with a sum of lorentzians. The sum of lorentzians can be expressed as:

$$f(E) = \frac{1}{E_2 - E_1} \int_{E_1}^{E_1} \frac{fwhm}{2} \frac{1}{(E - E_0)^2 + (\frac{fwhm}{2})^2} dE_0 \tag{A.3}$$

that gives

$$f(E) = \frac{1}{\pi(E_2 - E_1)} \left[ -\arctan \frac{E - E_2}{\frac{fwhm}{2}} + \arctan \frac{E - E_1}{\frac{fwhm}{2}} \right] \tag{A.4}$$

where $fwhm$ is the full width at half maximum of the single $k_{\|}$-lorentzian, that is considered constant in the $k_{\|}$ range, $E_0$ is the energy position of the lorentzian, $E_1 = \hbar^2(k_{\|} - \Delta k_{\|})^2/2m$ and $E_2 = \hbar^2(k_{\|} + \Delta k_{\|})^2/2m$. Using this fitting procedure the intrinsic IPS linewidths at $k_{\|}$=0 are in agreement with the previous results, confirming that the $k_{\|}$-spread is not relevant at $k_{\|}$=0. The intrinsic linewidths at $k_{\|} \neq 0$ result the same, within the errors, for both high and low resolution ToF (Fig. 3.2 (b,d)). The slope of the solid lines which represents the best linear fit of the IPS linewidths versus $E_{\|}$ is 120 30meV/eV and 115 30meV/eV for high and low resolution ToF, respectively. This slope is comparable with the slope obtained by the high resolution ToF using the single lorentzian fit (150 40meV/eV). Therefore, the contribution of the $k_{\|}$-spread in the IPS intrinsic linewidth measurement, can be neglected when the geometrical angular acceptance of the ToF implies a $k_{\|}$-spread of about 0.015 $\mathring{A}^{-1}$.

The measured slope of the linewidth broadening in Ag(100) as a function of $E_{\|}$ ($d\Gamma /dk_{\|}$=120 meV/eV) gives an interesting hint when compared to the inverse lifetime ($\gamma$=$\hbar/\tau$ ) broadening measured on Cu(100) using time-resolved 2PPE ($d\Gamma /dk_{\|}$=47 meV/eV) [22]. Theoretical calculations for Cu(100) evidence that the contribution of *intraband* scattering must be taken into account to reconcile theory with the measured value of inverse lifetime vs parallel momentum broadening rate. In Ag(100) we find a much more rapid broadening rate, indicating that a different decay dynamics must be considered in evaluating the IPS relaxation in this case. This finding can be related to the presence of a collective excitation (surface plasmons) in Ag(100) that constitutes an important decay channel for IPS. At $k_{\|}$=0, the surface plasmon contribution to the decay of Ag(100) IPS is greatly diminished due to a subtle effect originating from the non-local character of the electronic self-energy [24], resulting in a longer lifetime of the IPS than would be expected considering the plasmon decay channel without the non-local correction. The high linewidth broadening rate measured in this work is consistent with a less effective quenching mechanism of the surface plasmon decay channel due to nonlocality at $k_{\|}$≠0. Another possible contribution to the different linewidth broadening could be an increase with parallel momentum of

quasi-elastic processes. These mechanisms can influence inverse linewidth estimations, while do not contribute to lifetime measured by pump-probe techniques.

# Appendix B

# Acronyms

| | |
|---|---|
| AB | Aharonov-Bohm |
| AFM | Atomic force microscopy |
| ARPES | Angle Resolved Photoemission Spectroscopy |
| ATI | Above-threshold ionization |
| ATP | Above-threshold photoionization |
| BE | Binding energy |
| DI | Deionized water |
| DIL | Dual in line |
| DOS | Density-of-states |
| EBL | Electron-beam lithography |
| FD | Fermi-Dirac |
| FET | Field-effect transistor |
| IPA | Isopropylic alchool |
| IPS | Image Potential State |
| LED | Light emitting diode |
| LEED | Low-energy electron diffraction |

| | |
|---|---|
| MBE | Molecular beam epitaxy |
| PMMA | Polymethyl-methacrylate |
| QD | Quantum dot |
| OC | Ohmic cntact |
| QH | Quantum Hall |
| QW | Quantum wire |
| SB | Schottky barrier |
| SBZ | surface Brillouin zone |
| ToF | Time-of-flight |
| TOPG | Travelling-wave optical parametric generator |
| UHV | de Ultra-high vacuum |
| 1D | One-dimensional |
| 2D | Two-dimensional |
| 3D | Three-dimensional |
| 2DEG | Two Dimensional Electron Gas |
| 2PPE | Two Photon Photoemission Spectroscopy |

# Bibliography


[1] D. Straubb and F. J. Himpsel, Phys. Rev. B **33**, 2256 (1986).

[2] P. M. Echenique and J. B. Pendry, Prog. Surf. Sci. **32**, 111 (1990).

[3] P. M. Echenique and J. B. Pendry, J. Phys. C **11**, 2065 (1978).

[4] U. Höfer, I. L. Shumay, C. Reuß, U. Thomann, W. Wallauer, and T. Fauster, Science **277**, 1480 (1997).

[5] T. Fauster and W. Steinmann, Appl. Phys. Lett. **68**, 418 (1996).

[6] R. Dingle, H. L. Stormer, A. C. Gossard, and W. Wiegman, **33**, 65 (1978).

[7] C. Weisbuch and B. Vinter, *Quantum Semiconductor Structure* (Academic Press, San Diego, 1991).

[8] G. Timp, A. Chang, J. Cunningham, T. Y. Chang, P. M. R. Behringer, and R. E. Howard, Phys. Rev. Lett. **58**, 2814 (1987).

[9] S. Datta, M. Melloch, S. Bandyopadhyay, R. Norem, M. Vaziri, M. Miller, and R. Reifenberger, Phys. Rev. Lett. **55**, 2344 (1985).

[10] D. K. Ferry and S. M. Goodnick, in *Transport in Nanostructures*, edited by M. P. H. Ahmed and A. Broers (Cambridge Univeristy Press, Cambridge, 1997), pp. 124–131.

[11] R. Landauer, IBM J.Rev.Dev. **1**, 223 .

[12] F. Capasso, *Physics of Quantum Electron Devices* (Springer, Berlin, 1990).

[13] J. Rundgren and G. Malstrm, Phys. Rev. Lett. **38**, 836 (1977).

[14] P. Johnson and N. Smith, Phys. Rev. B **27**, 2527 (1983).

[15] G. Binning, K. Frank, H. Fuchs, N. Garcia, B. Reihl, H. Roeher, F. Salvan, and A. Williams, Phys. Rev. Lett. **55**, 991 (1985).

[16] K. Giesen, F. Hage, F. J. Himpsel, H. J. Riess, and W. Steinmann, Phys. Rev. Lett. **55**, 300 (1985).

[17] G. Ferrini, C. Giannetti, D. Fausti, G. Galimberti, M. Peloi, G. P. Banfi, and F. Parmigiani, Phys. Rev. B **67**, 235407 (2003).

[18] R. Schoenlein, J. Fujimoto, G. Eesley, and T. Capehart, Phys. Rev. B **41**, 5436 (1990).

[19] I. Shumay, U. Hfer, C. Reu, U. Thomann, W. Wallauer, and T. Fauster, Phys. Rev. B **58**, 13974 (1998).

[20] C. Reu, I. Shumay, U. Thomann, M. Kutschera, M.Weinelt, T. Fauster, and U. Hfner, Phys. Rev. Lett. **82**, 153 (1999).

[21] A. Miller, I. Bezel, K. Gaffney, S. Garret-Roe, S. Liu, P. Szymanski, and C. Harris, Science **297**, 1163 (2002).

[22] W. Berthold, U. Hfer, P. Feulner, E. Chulkov, V. Silkin, and P. Echenique, Phys. Rev. Lett. **88**, 056805 (2002).

[23] K. Boger, M. Roth, M. Weinelt, T. Fauster, and P. Reinhard, Phys. Rev. B **65**, 075104 (2002).

[24] A. García-Lekue, J. M. Pitarke, E. V. Chulkov, A. Liebsch, and P. M. Echenique, Phys. Rev. Lett. **89**, 096401 (2002).

[25] M. Wolf, A. Hotzel, E. Knoesel, and D. Velic, Phys. Rev. B **59**, 5926 (1999).

[26] R. W. Schoenlein, J. G. Fujimoto, G. L. Eesley, and T. W. Capehart, Phys. Rev. Lett. **61**, 2596 (1988).

[27] G. Paolicelli *et al.*, Surf. Rev. and Lett. **9**, 541 (2002).

[28] W. S. Fann, R. Storz, and J. Bokor, Phys. Rev. B **44**, 10980 (1991).

[29] G. Farkas, C. Toth, S. D. Moustaizis, N. A. Papadogiannis, and C. Fotakis, Phys. Rev. A **46**, 3605 (1992).

[30] H. Ehrenreich and H. R. Phillip, Phys. Rev. **128**, 1622 (1962).

[31] T. Fauster and W. Steinmann, in *Two-photon photoemission spectroscopy of image states*, Vol. 2 of *Electromagnetic Waves: Recent Development in Research*, edited by P. Halevi (Elsevier Science B. V., Amsterdam, 1995), Chap. 8, p. 347.

[32] P. Agostini, F. Fabre, G. Mainfray, and G. Petite, Phys. Rev. Lett. **42**, 1127 (1979).

[33] T. J. McIlrath, P. H. Bucksbaum, R. R. Freeman, and M. Bashkansky, Phys. Rev. A **35**, 4611 (1987).

[34] R. Freeman, P. Bucksbaum, H. Milchberg, S. Darack, D. Schumacher, and M. Geusic, Phys. Rev. Lett. **59**, 1092 (1987).

[35] G. D. Gillen and L. D. V. Woerkom, Phys. Rev. A **68**, 033401 (2003).

[36] M. J. Dewitt and R. Levis, Phys. Rev. Lett. **81**, 5101 (1998).

[37] S. Luan, R. Hippler, H. Schwier, and H. O. Lutz, Europhys. Lett. **9**, 489 (1989).

[38] W. S. Fann, R. Storz, and J. Bokor, Phys. Rev. B **44**, 10 .

[39] G. Farkas and C. Toth, Phys. Rev. A **41**, 4123 (1990).

[40] L. V. Keldysh, Sov. Phys. JETP **20**, 1307 (1965).

[41] Johnson and R. Christy, Phys. Rev. B **6**, 4370 (1972).

[42] G. P. Banfi, G. Ferrini, M. Peloi, and F. Parmigiani, Phys. Rev. B **67**, 035428 (2003).

[43] F. H. M. Faisal, *Theory of Multiphoton Processes* (Plenum, New York, 1987).

[44] Z. Li and S. Gao, Phys. Rev. B **50**, 15 .

[45] P. B. Corkum, N. Burnett, and F. Brunel, Phys. Rev. Lett. **62**, 1259 (1989).

[46] Y. Aharonov and D. Bohm, Phys. Rev. **115**, 485 (1959).

[47] K. K. Choi, D. C. Tsui, and K. Alavi, Phys. Rev. B **36**, 7751 (1987).

[48] J. Liu, K. Ismail, K. Y. Lee, J. M. Hong, and S. Washburn, Phys. Rev. B **47**, 13039 (1993).

[49] S. Pedersen, A. E. Hansen, A. Kristensen, C. B. Sørensen, and P. E. Lindelof, Phys. Rev. B **61**, 5457 (2000).

[50] Y. Ji, Y. Chung, D. Sprinzak, M. Heiblum, D. Mahalu, and H. Shtrikman, Nature **422**, 415 (2003).

[51] A. E. Hansen, A. Kristensen, S. Pedersen, C. B. Sørensen, and P. E. Lindelof, Phys. Rev. B **64**, 045327 (2001).

[52] A. Yacoby, R. Schuster, and M. Heiblum, Phys. Rev. B **53**, 9583 (1996).

[53] S. Roddaro, V. Piazza, F. Beltram, W. Wegscheider, C. Liang, and M. Pepper, J. Appl. Phys. **92**, 5304 .

[54] V. Piazza, F. Beltram, W. Wegscheider, C. Liang, and M. Pepper, Phys. Rev. B **62**, 10630 .

[55] S. Pedersen, A. E. Hansen, A. Kristensen, C. B. Sørensen, and P. Lindelof, J. Low Temp. Phys. **118**, 457 (2000).

[56] A. E. Hansen, S. Pedersen, A. Kristensen, C. B. Sørensen, and P. E. Lindelof, Physica E **7**, 776 (2000).

[57] A. K. Geim, S. V. Dubonos, J. G. S. Lok, I. V. Grigorieva, C. M. J, L. T. Hansen, and P. E. Lindelof, Appl. Phys. Lett. **71**, 2379 (1997).

[58] V. V. Mitin, V. A. Kochelap, and M. A. Stroscio, *Quantum Heterostructyres* (Cambridge University Press, Cambridge, 1999), p. 393.

[59] S. Datta, M. Melloch, S. Bandyopadhyay, and R. Noren, Appl. Phys. Lett. **55**, 2344 .

[60] S. Datta, M. Melloch, S. Bandyopadhyay, and M. S. Lundstrom, Appl. Phys. Lett. **48**, 487 (1986).

[61] M. Okuda, K. Fujiii, and A. Shimizu, Appl. Phys. Lett. **57**, 2231 (1990).

[62] J. A. Alamo and C. C. Eugster, Appl. Phys. Lett. **56**, 78 (1990).

[63] C. C. Eugster, J. A. Alamo, M. J. Rooks, and M. R. Melloch, Appl. Phys. Lett. **60**, 642 (1992).

[64] C. C. Eugster, J. A. Alamo, M. J. Rooks, and M. R. Melloch, Appl. Phys. Lett. **64**, 3157 (1994).

[65] V. Piazza, P. Casarini, S. D. Franceschi, M. lazzarino, F. Beltram, C. Jacoboni, A. Bosacchi, and S. Franchi, Phys. Rev. B **57**, 10017 (1998).

[66] W. M. Moreau, *Semiconductors Lithography, Principles, Practices and Materials* (Plenum Press, New York, 1998).

[67] M. A. McCord and M. J. Rooks, in *Handbook of Microlithography, Micromachining and Microfabrication*, edited by P. Rai-Choudhury (SPIE Optical Engineering Press, Bellingham, WA, U.S.A, 1997).

[68] M. Madou, *Fundamentals of Microfabrication* (CRC Press, Boca Raton, USA, 1997).

[69] M. J. Kelly and C. Weisbuch, *The Physics and Fabrication of Microstructures and Microdevices. Part 1* (Academic Press, San Diego, 1986).

# List of publications

♣ *Interface roughness effects in Gaussian superlattices* , F. Banfi, V. Bellani, I. Gomez, E. Diez and F. Domnguez-Adame, Semicond. Sci. Technol. **16**, 304 (2001).

♣ *Design of a multiple ring AharonovBohm gradiometer*, Francesco Banfi, Semicond. Sci. Technol. **19**, 342 (2004).

♣ *Measurements of $k_{\|}$-dependent intrinsic linewidth of image-potential states on Ag(100)*, C. Giannetti, G. Galimberti, S. Pagliara, G. Ferrini, F. Banfi, D. Fausti, and F. Parmigiani, acceped to be published on Surf. Science.

♣ *Violation of the electric dipole selection rules in indirect multiphoton excitation of image potential states on Ag(100)*, G. Ferrini, C. Giannetti, G. Galimberti, S. Pagliara, D. Fausti, F. Banfi and F. Parmigiani, submitted to Phys. Rev. Lett.

♣ *Experimental evidence of above-threshold photoemission in solids*, F. Banfi, C. Giannetti, Ferrini, G. Galimberti, S. Pagliara, D. Fausti, and F. Parmigiani, submitted to Phys. Rev. Lett.

# Acknowledgements

*This thesis is the outcome of a three years experience that involved many more people than myself. First of all I want to thank my dad, papà for me, il Lungo for friends and Professor Giampiero Banfi for many others. E' riduttivo dedicarti questa tesi papà, infinitamente riduttivo perchè ti devo molto di più e in ambiti ben più importanti, tuttavia sò che apprezzeresti, per mille motivi, la conclusione di questo lavoro. Grazie papà. I want to thank Professor Fulvio Parmigiani, both as an eclectic Professor and as an enlighting scientific guide, but, overall, as a great man. Grazie Fulvio, grazie di essermi stato vicino nei momenti duri, supportato nelle necessità della vita e di aver condiviso a pieno cuore i momenti felici. Grazie per le brain storming sessions del venerdì e per avermi fatto conoscere lo strolghino, meglio noto come 'strulghen', e l'Ortrugo. I aknowledge Professor Giorgio Guizzetti for supervising the 'broad' scheme during my movements. I want to aknowledge the Elphos group in Brescia for their inconditionate support. Grazie Daniele la sciata in notturna. Grazie Claudio, non prolisso ma sempre efficacie. Grazie Gabriele (a quante birre siamo?), Stefania e Gianluca. For the same reasons I want to aknowledge the NEST group in Pisa. Grazie Paskà e Rod. Mi avete insegnato tanto e sempre con passione. Grazie Vince, Franky, Michele e Luos. Grazie Cesar, sempre pronto ad un sorriso, al 'tranquilo che se sestema tuto', 'la tortilla è pronta' e quant'altro. Grazie Aldone 'linea retta', burbero e schietto anche senza vino. Grazie Kasper per le notti passate a discutere. Non potrò mai rendevi le ore di sonno che vi devo per i transfers d'elio e quant'altro. Grazie Riccardo per il fondamentale ausilio informatico prestatomi alle ore più improbabili, e per avere recuperato i files di questa tesi innumerevoli volte. Peccato però tu non corra. Grazie Lagio per avermi ospitato senza avermi mai conosciuto prima e per la cozzata. A thesis work is just one part of life and life sometimes strikes hard. In tough moments issues other than a thesis work have to be dealt with. This was my case and no time would have been left for research without the warm support of some great people. Grazie Sergio, Alberto, Laura, Luca, Maurizio, Tina, Bernasconi tutti e Thierr. Over all my sister Ludovica deserves a special thank for reasons hard to explain here. Grazie Ludo!*